Local blade whirl and global rotor whirl interaction

Thirstrup Petersen, J.; Thomsen, K.; Aagaard Madsen, Helge

Publication date:
1998

Document Version
Publisher's PDF, also known as Version of record

RISØ

Risø-R-1067(EN)

Local Blade Whirl and Global Rotor Whirl Interaction

Jørgen Thirstrup Petersen, Kenneth Thomsen, Helge Aagaard Madsen

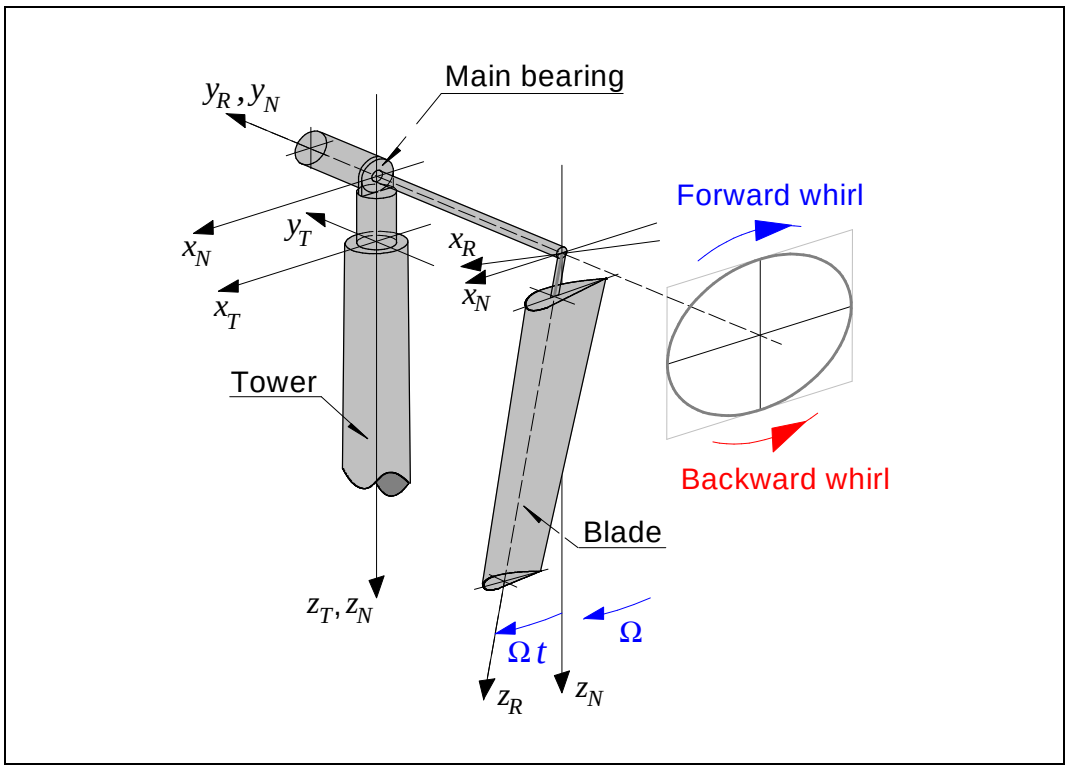

Risø National Laboratory, Roskilde, Denmark
August 1998

Abstract Investigation of stall induced vibrations has shown that the actual value of the edgewise blade frequency relative to the coupled, global rotor tilt-yaw frequencies is important for development of the vibrations. They develop more easily if the blade frequency is close to one of the rotor tilt-yaw frequencies referred to common coordinates. This observation indicates that an important coupling exists between the blade edgewise modes and the global rotor modes. The presented work aims at providing insight into the physics of this coupling by use of simple models, which take into account the effects believed to be most important in the considered state of operation. We assume that the dominating inertia force on the blades originates from the edgewise vibration. The resulting inertia force at the hub, which turns out to be a force rotating in the rotor plane with the edgewise frequency, is then considered as the forcing on the supporting structure, i.e. the main shaft, the nacelle frame and the tower. A four degrees of freedom model of the rotor and the supporting structure is used to illustrate the global rotor tilt-yaw mode shapes during operation. A mathematical model for the work performed by the inertia force from the blade vibration on the hub movement shows, how energy might be exchanged between the structural elements. In addition, full aeroelastic calculations are used to support and extend the conclusions from the simple models, when the complex, real wind turbine structure is considered. The in-plane inertia force describes an elliptical path in the rotor plane, and we denote the corresponding blade deformation *local blade whirl*. Likewise, the hub moves along an elliptical orbit, when the rotor tilt-yaw modes are excited, and we denote this movement *global rotor whirl*. Using these terms our concern is the interaction between *local blade whirl* and *global rotor whirl*. The models are used to illustrate the findings through examples. It is concluded that not only should the local blade whirl frequencies and the global rotor whirl frequencies be separated as much as possible, but certain frequency intervals should be avoided as well. Although the work is inspired by analysis on stall regulated wind turbines, the dynamic principles are equally valid for turbines with any type of regulation.

Research funded by The Danish Ministry of Energy through the project *Program for forskning i aeroelasticitet*, EFP-97 contract ENS-1363/97-0002.

ISBN 87–550–2418–1
ISBN 87–550–2420–3 (Internet)
ISSN 0106–2840

Information Service Department · Risø · 1998

Table of contents

Preface

Results are presented from structural dynamics research, which has been carried out at Risø within the program *Aeroelastic Design*. The work is a contribution to one of the tasks in the EFP-97 project *Program for forskning i aeroelasticitet*. The specific task is concerned with

- Identification of main parameters for load reduction.

The research is inspired by previous work in projects concerned with investigation of stall induced vibrations. These projects are the national EFP-96 project *Kantsvingninger i stall* and the international EC Joule-III project *Prediction of Dynamic Loads and Induced Vibrations in Stall* [1].

A summary of the results from the present work is included in the final report for the EFP-97 project, Risø-R-1066(DA), *Forskning i Aeroelasticitet. EFP-97 Slutrapport* [2].

1 Introduction

In connection with investigation of stall induced edgewise blade vibrations [1] on three bladed stall regulated wind turbines it has been observed that the actual values of the rotor tilt-yaw frequencies relative to the edgewise blade frequency are important for the development of the stall induced vibrations. Measurements and simulations with aeroelastic codes show that the edgewise vibrations develop more easily if the blade frequency is close to either of the rotor tilt-yaw frequencies, assuming that the frequencies are referenced to a common coordinate system.

This observation indicates that an important coupling exists between the blade vibration and the global rotor tilt-yaw modes. The present report describes the physical nature of this coupling partly by use of simple models and partly by use of full aeroelastic calculations. The simple models consider only the dynamic effects, which we believe are the most dominating, and neglect wind and gravity loads. Basically, the rotor and the rotor support are considered as two separate structures, which interact at the rotor hub. The aeroelastic calculations use models, which have a very detailed representation of both loads and structural elements, and the calculations are capable of simulating the behaviour of the real turbine with good accuracy.

In the simple models we assume that the blades vibrate in the natural edgewise mode shapes and that the inertia force from this movement dominates the total inertia force. The force from the blades as seen by the shaft will be the resulting inertia force from the edgewise vibration. The aim is to investigate the response of the coupled wind turbine structure, when it is excited by this force.

A simple model of the wind turbine with only four degrees of freedom at the tower top and the main bearing support is applied to illustrate the global behaviour of the wind turbine during operation. In this model all the rotating parts, including the blades, are considered completely rigid. The included degrees of freedom approximate the dominating degrees of freedom for the turbine structure, when the tilt-yaw mode shapes are excited during operation. It turns out that the rotor center in these modes moves along an elliptical path.

A mathematical model is used to account for the energy exchange between the blade vibrations and the global rotor vibrations. The model calculates the work performed by the inertia force from the blade vibration on the rotor hub, when the blade vibration takes place simultaneously with the tilt-yaw mode shape deformation.

The findings and the conclusions from the simple models are supported by general aeroelastic calculations, which are believed to have an adequate representation of the degrees of freedom relevant for a real wind turbine. In the aeroelastic code the different degrees of freedom can be locked, and by doing so the simulations can be used to support the conclusions drawn from the results obtained with the simple models mentioned above, as the simulations approach the behaviour of the simple model. Furthermore, the use of a full aeroelastic code for identification of the global rotor tilt-yaw modes for a flexible turbine during operation is demonstrated.

An example turbine

Throughout the presented work we use numerical examples to show the order of magnitude of the different deformations and loads. For this purpose an example wind turbine is used, which represents the typical Danish, 3-bladed, stall regulated, 500 kW type with 19.0 m blades. This turbine is further used to illustrate the mode shapes, which participate in the dynamic phenomena under investigation. The main data for the turbine are presented in Section 2.

Initially, the natural frequencies and the mode shapes are calculated for the whole turbine at stand still without simplifying assumptions. The frequencies are listed and the associated mode shapes described in Section 2.1, where also three fundamental mode shapes involved in the dynamic interaction phenomenon are shown and described.

The presented mode shape calculations and the later time simulations are carried out by use of the Risø aeroelastic code HawC described in detail in [3] and in overview in [4]. The HawC model is believed to have a satisfactory representation of the mode shapes involved.

In-plane inertia force – local blade whirl

By assuming that the blades vibrate in the edgewise mode shapes, we illustrate how an inertia force develops in the rotor plane giving rise to a rotating moment at the tower top and at the main bearing. This moment might interact with the rotor tilt-yaw mode shapes, when certain conditions are present regarding the actual frequencies of the involved modes.

In Section 3.1 the derivation of the in-plane inertia force, resulting from the vibration in the edgewise mode shapes, is presented. The appearance of the force in both rotating coordinates (fixed in the rotor) and stationary coordinates (fixed in the tower) is shown. The force rotates with the blade edgewise frequency and describes an elliptical orbit in the rotating coordinates (see Figure 3.4). Elliptical orbits are typical deformation patterns, e.g. for flexible shafts in different turbomachines, and the term *whirl* is used for this type of motion. Therefore, we choose to use the term *local blade whirl* for the blade deformations corresponding to the rotating force, and *local* as opposed to the term *global whirl*, which we intend to use for the movement of the hub during excitation of the rotor tilt-yaw modes.

The force can be decomposed in two counter-rotating components, which both describe a circular orbit, and both rotate with the blade frequency. This decomposition is presented in Section 3.2.

Theory is presented in Section 3.3, demonstrating how a simulated or a measured response can be decomposed using the presented methods, which until this point assume that the blade deformation in each of the mode shapes is known a priori.

Rotor tilt-yaw mode shapes – global rotor whirl

A simple four degrees of freedom model of the wind turbine is presented in Section 4. The purpose of this model is to show, how the frequencies of the tilt-yaw mode shapes change with the rotational speed of the rotor and to illustrate these mode shapes during operation. In the model the rotating parts, including the blades, are considered completely rigid.

Basically, the four degrees of freedom model takes into account the flexibility of the rotor support. Two springs are located at the tower top and two at the main bearing support. Each spring has a rotational degree of freedom, allowing the rotating shaft to change direction in space, corresponding to a movement of the rotor center in a vertical plane. This movement of the shaft during operation approximates the movement in the rotor tilt-yaw mode shapes for a flexible turbine. The homogeneous equations of motion are solved explicitly with respect

to natural frequencies, and the influence of rotational speed on the frequencies due to change of gyroscopic forces is illustrated.

When one of the rotor tilt-yaw modes are excited, the movement of the rotor center in the vertical plane follows an elliptical path (see Figure 4.1), and based on the same ideas as above for the in-plane force we choose to denote this movement *global rotor whirl*. Using these terms our concern is the interaction between *local blade whirl* and *global rotor whirl*.

Examples demonstrating the methods

The models and the theory are used in examples to illustrate the findings throughout the sections, where the theory is presented. The examples are based on an imaginary 3-bladed, stall regulated, 500 kW wind turbine equipped with 19.0 m blades. Further, general aeroelastic simulations are used to illustrate the behaviour of a wind turbine in normal stalled operation. The results are presented in Section 5.

Mathematical model for exchange of energy

The interaction between the structural components is rather complex for a real, flexible turbine, and the interpretation of the results obtained by full aeroelastic calculations is rather difficult. This interpretation is supported by a mathematical model, which accounts for the work performed by the in-plane inertia force due to blade vibration on the hub movement, when the global rotor whirl modes are excited. This model is presented in Section 6.

Global rotor whirl modes for a flexible turbine

In a design situation it might be valuable, if the frequencies involved in the present coupling phenomenon can be predicted, as this gives the designer the opportunity to control – to some extent – the final design frequencies and the dynamic behaviour. As shown in Section 2.1 the frequencies can be determined at stand still by solving the equations of motion in the aeroelastic model. At present, this is not possible for a rotating wind turbine, and as the frequencies might change considerably compared to the stand still case, other methods must be looked for. In general, the blade edgewise frequency is easy to determine, for instance from the power spectral density of the blade root bending moment during operation. The determination of the global rotor whirl frequencies is less straightforward. The simple four degrees of freedom model mentioned above is not well suited for determination of the global whirl frequencies for a real, flexible turbine, because the simplification involves approximations to the real structure. A method based on simulation with an aeroelastic code is presented in Section 7. The method makes use of external, harmonic excitation, and the frequencies are determined from the response.

2 The example wind turbine

In the examples presented in later sections an imaginary wind turbine is applied. It is assumed to represent the typical 3-bladed, Danish, stall-regulated concept, but the described dynamic principles are equally valid for turbines with any type of power regulation.

The main data for the example wind turbine, relevant for the analysis below, are listed in Table 2.1. The actual distributed stiffnesses and masses are not shown, except the blade mass, which enters the later calculations. The blade mass distribution is shown in Figure 2.1.

Still, the structural data applied in the aeroelastic model are chosen to give realistic natural frequencies and mode shapes. The calculated frequencies and mode shapes at stand still are presented in Section 2.1.

Table 2.1. Main data for the example 500 kW turbine with 19.0 m blades.

Component	Parameter	Value
Rotor	Number of blades	3
	Rotor diameter	41.0 m
	Hub height	40.0 m
	Rotor overhang	2.00 m
	Rotor speed at rated power, 1P, $\Omega \simeq$	30.0 rpm, 0.5 Hz, 3.142 rad/sec

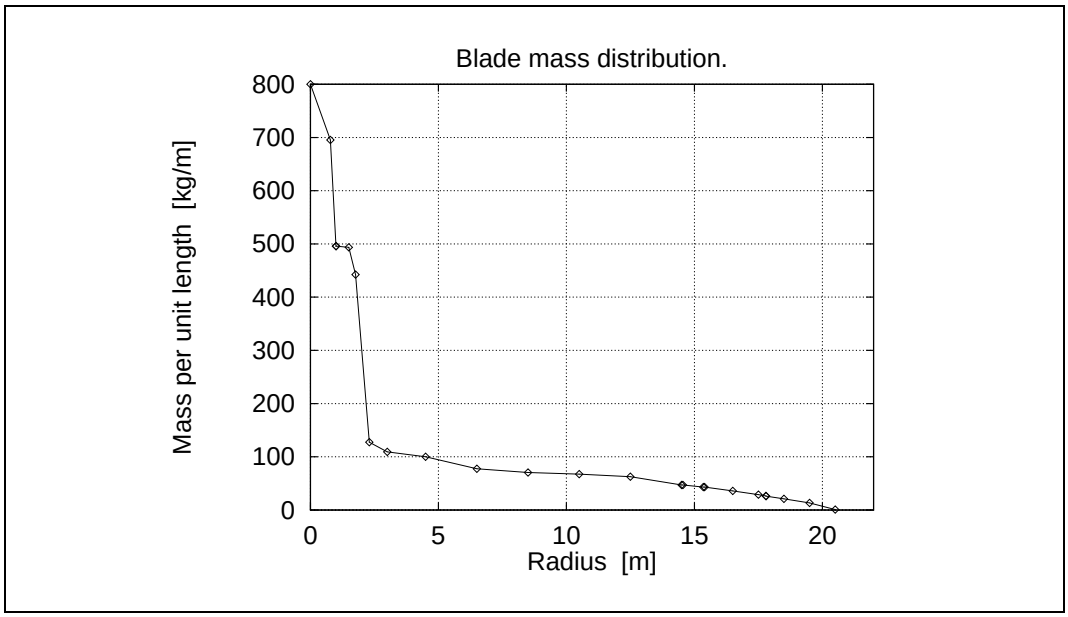

Figure 2.1. Blade mass distribution.

2.1 Mode shapes and natural frequencies

The simulated natural frequencies at stand still are listed in Table 2.1. The Si1 case covers the basic turbine, and the Si2 case covers a turbine with stiffened shaft. The latter is used to demonstrate the influence of structural modifications on the global rotor whirl modes. In the table short descriptions of the actual modes are given as well.

Especially two modes are of importance for edgewise vibrations, namely node number 7 and mode number 8. Mode number 7 is shown in Figure 2.2. In this mode one blade, in the figure denoted blade 1, is practically at rest, and the other two, blade 2 and blade 3, are vibrating in counter-phase with identical amplitude. Mode number 8 is shown in Figure 2.3. Here one blade, blade 1, is vibrating in counter-phase with the other two, blade 2 and blade 3, which have half the amplitude of blade 1. Both mode 7 and 8 can be characterized as isolated rotor modes, in the sense that practically no coupling to the shaft torsional degree of freedom is present, as the inertia forces on the blades are dynamically in equilibrium with respect to moment about the main shaft axis. Still, they are both coupled to the shaft bending modes and through that to the rotor tilt-yaw modes, as the inertia forces on the blades are not dynamically balanced in the rotor plane, and a resulting harmonic inertia force will exist in the rotor plane. This is investigated and described in further detail in Section 3. The two edgewise modes have almost the same frequency, close to 2.9 Hz. The frequencies are only different because the rotor tilt and yaw stiffnesses are. If the tilt and the yaw stiffnesses are identical, the natural frequencies are found as a double root in the characteristic equation, and any linear combination of mode 7 and mode 8 will then be a mode shape as well. In this case no preferred directions exist, and any edgewise rotor mode could be described as a superposition of the two basic modes shown in the figures, possibly including a phase shift between the two. An appropriate linear combination of the modes shown could for instance transform the mode shapes to two new, where a different blade would be the blade at rest in mode 7. But still, only two mode shapes and natural frequencies exist. The fulfillment of the orthogonality condition for the mode shapes lies behind this statement. When the turbine rotates, the two frequencies are no longer distinct, and the analysis in Section 3 considers them as coinciding. The actual deformation vectors for both the edgewise and the flapwise mode shapes are illustrated by their polar coordinate components in Figure 2.1 as function of radius.

The rotor tilt and yaw modes – modes 4,5,9 and 10 – are the ones, which might participate in a coupled vibration with the edgewise blade modes. The 2^{nd} yaw mode – mode number 9 – is shown in Figure 2.4. The vertical blade is practically at rest, and the other two vibrate primarily in a flapwise direction in counter-phase with each other and in counter-phase with the nacelle.

When the turbine rotates, the frequencies of the tilt and yaw modes are changed compared to the ones listed in Table 2.1 due to the influence of the inertia forces, for instance centrifugal and gyroscopic forces, and the modes become tilt-yaw modes, referring to the fact that deformations in both tilt and yaw direction are usually present in a rotating mode, corresponding to one whirl frequency. The influence of the gyroscopic forces is described in detail in Section 4 by use of the simple four degrees of freedom model with infinitely stiff shaft and blades.

The rotor tilt and yaw modes will combine to what we in the present context choose to denote *global rotor whirl modes*, where the rotor center describes an elliptical orbit in the stationary coordinates (see Figure 4.1). The elliptical orbit can be decomposed in two circular orbits. One of the circular orbits is travelled by the rotor center in the same direction as the rotor rotates – we denote this component either *forward* or *progressive* whirl – and the other is travelled in the opposite direction – we denote this component either *backward* or *retrograde*

whirl. Accordingly, the resulting elliptical orbit might be travelled in *forward* or *backward* direction, depending on the actual size of the circular components. The basic principles of decomposing an elliptical orbit in its circular components are described in further detail in Section 3.

In Section 4 examples of global rotor whirl frequencies obtained by the simple four degree of freedom model for typical turbines with 19 m blades are shown in Figures 4.2 and 4.3. In this case it turns out that the lower of the 1^{st} tilt-yaw whirl frequencies decreases with rotor speed, and that the whirl direction is backward. Accordingly, the higher of the 1^{st} tilt-yaw whirl frequencies increases with rotor speed, and the whirl direction is forward. The same characteristics are observed for 2^{nd} tilt-yaw whirl frequencies as well, although their dependency on the rotor speed is less pronounced. The identification of the global whirl modes is further addressed in Section 7, where a general aeroelastic code is used to identify the modes.

Table 2.1. Simulated natural frequencies at stand still. The Si1 *case covers the basic turbine and the* Si2 *case covers a turbine with stiffened shaft.*

Frequency number	Case Si1: Simulated frequency [Hz]	Case Si2: Simulated frequency [Hz]	Description of mode
1	0.760	0.760	Tower across wind
2	0.807	0.808	Tower along wind
3	0.905	0.905	Shaft torsion
4	1.363	1.462	1^{st} rotor yaw
5	1.575	1.711	1^{st} rotor tilt
6	1.852	1.854	1^{st} blade flapwise
7	2.916	2.922	1^{st} blade edgewise, Figure 2.2
8	2.964	2.973	1^{st} blade edgewise, Figure 2.3
9	3.668	3.756	2^{nd} rotor yaw, Figure 2.4
10	4.360	4.965	2^{nd} rotor tilt

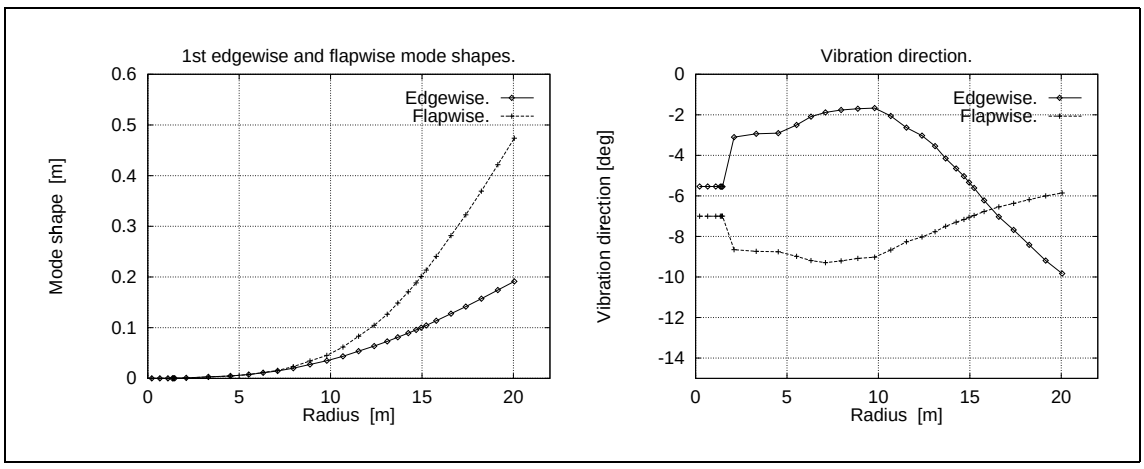

Figure 2.1. Mode shape vector size (left) and vibration direction angle, θ_{RB} (right). The angle is defined in Figure 2.5. The flapwise direction is plotted with an offset of $\Delta\theta_{RB} = -90°$.

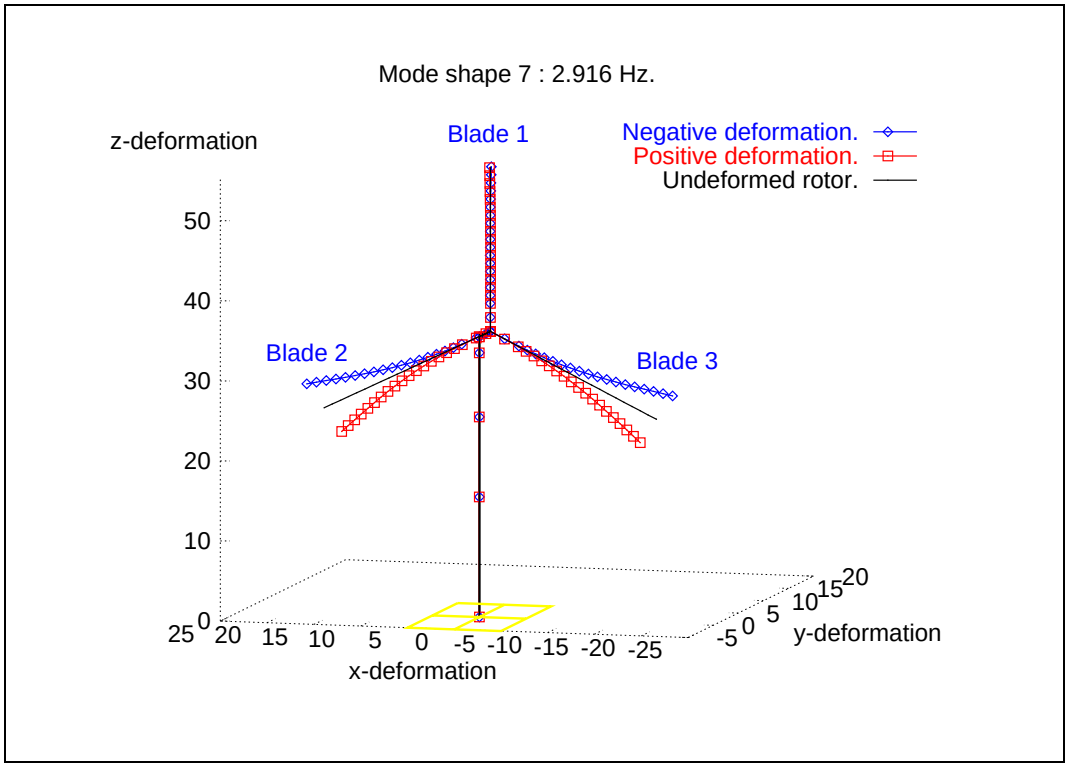

Figure 2.2. Edgewise mode shape number 7.

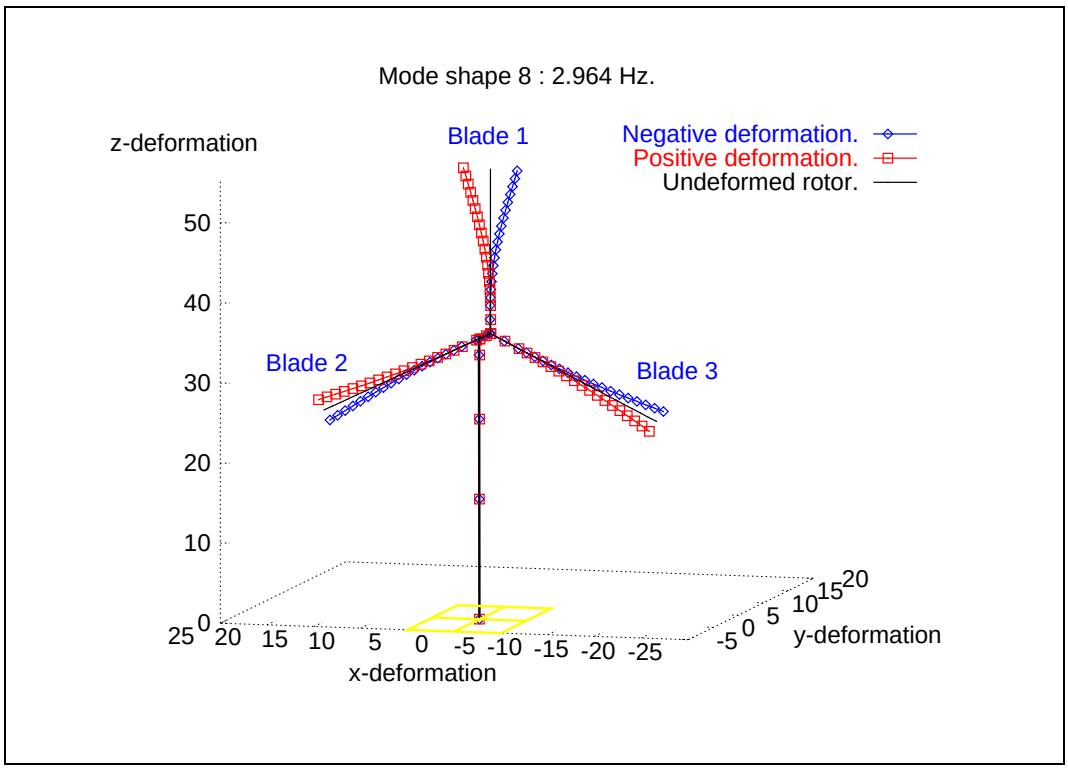

Figure 2.3. Edgewise mode shape number 8.

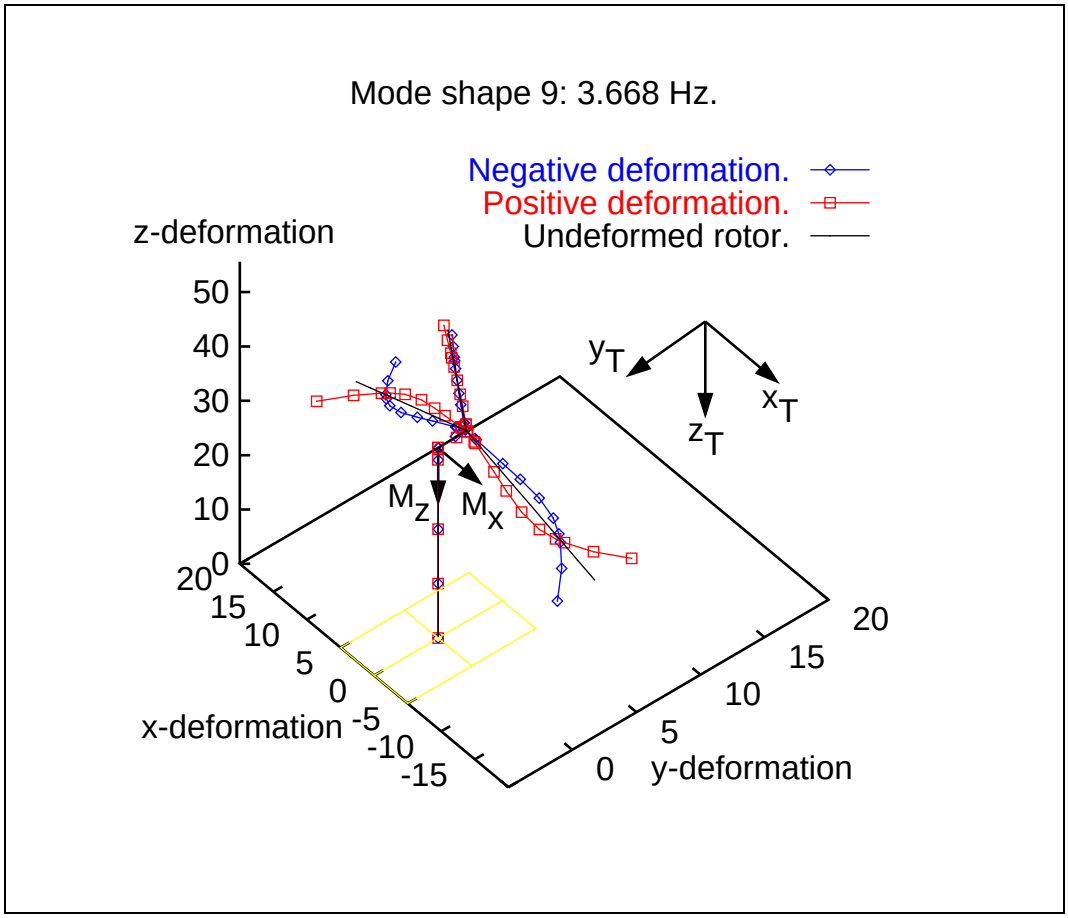

Figure 2.4. 2^{nd} rotor yaw mode shape. The moment components, M_x and M_z, are used for excitation of the global rotor whirl modes as presented in Section 7. The sign of the plot axis units is opposite to the orientation of the coordinates of the stationary tower coordinates, (x_T, y_T, z_T). See also Figure 4.1 in Section 4 for a definition of coordinate systems.

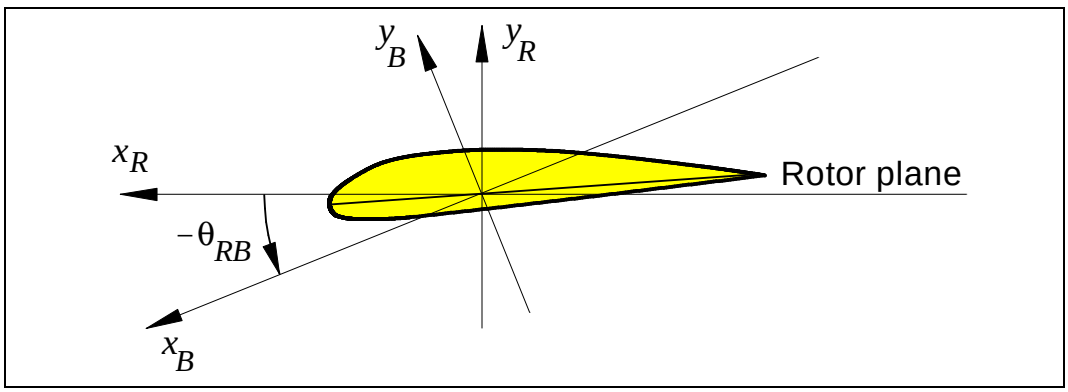

Figure 2.5. Definition of vibration direction angle, θ_{RB}.

3 Local blade whirl

Aeroelastic calculations and measurements on full scale wind turbines in operation show that there is a significant coupling between the *local edgewise blade modes* (also denoted the *local blade whirl modes*) and the *global rotor whirl modes*. Our definition of the global rotor whirl modes is presented in Section 4, where a simple four degrees of freedom model is used to illustrate examples. For instance, a change of component stiffness that results in a change of the separation between the values of the edgewise frequencies and the global whirl frequencies can change the edgewise vibration response significantly. From the calculations on the example wind turbine presented later in Section 5 it is observed that the closer the 2^{nd} backward rotor tilt-yaw whirl frequency is to the edgewise blade frequency referenced to the stationary coordinates, $\omega_e + \Omega$, the higher the edgewise vibration level will be. Change of the rotor whirl frequency towards higher values results in decreased vibration level. Typical values of the global rotor whirl frequencies are presented in Section 4, for example in Figure 4.3. As we show later in Section 6 by considering the energy exchange, not only the separation between the frequencies matters, but also their relative values are important, i.e. whether a rotor whirl frequency is below or above a blade edgewise whirl frequency in common reference coordinates. In the examples only the 2^{nd} rotor whirl frequencies seems to be close enough to the edgewise frequency to be important, but in general the 1^{st} rotor whirl frequencies should be considered as well.

The coupling between global rotor whirl modes and edgewise blade modes is complex, primarily due to flexibility of the structural elements, which are involved in the rotating modes. This flexibility has to be represented in a model, if the modeling of inertia forces – including gyroscopic forces – should be adequate. This is believed to be properly taken care of in the applied HawC aeroelastic code. However, we would like to get some better understanding of the coupling phenomenon by looking at a simple model of the blade inertia forces, which are believed to be the more important ones for the coupling. This model is presented below.

3.1 In-plane blade inertia force resulting from edgewise vibration

The deformations in the fundamental edgewise blade modes, i.e. modes 7 and 8 shown in Figures 2.2 and 2.3, respectively, are described by the orthogonal and normalized mode shape vectors

$$\{\varphi_7(r)\} = \left\{ \begin{array}{c} \varphi_{B1,7}(r) \\ \varphi_{B2,7}(r) \\ \varphi_{B3,7}(r) \end{array} \right\} = \varphi_B(r) \left\{ \begin{array}{c} a_{17} \\ a_{27} \\ a_{37} \end{array} \right\} = \varphi_B(r) \left\{ \begin{array}{c} 0 \\ \frac{1}{\sqrt{2}} \\ -\frac{1}{\sqrt{2}} \end{array} \right\} \tag{3.1}$$

and

$$\{\varphi_8(r)\} = \left\{ \begin{array}{c} \varphi_{B1,8}(r) \\ \varphi_{B2,8}(r) \\ \varphi_{B3,8}(r) \end{array} \right\} = \varphi_B(r) \left\{ \begin{array}{c} a_{18} \\ a_{28} \\ a_{38} \end{array} \right\} = \varphi_B(r) \left\{ \begin{array}{c} \frac{2}{\sqrt{6}} \\ -\frac{1}{\sqrt{6}} \\ -\frac{1}{\sqrt{6}} \end{array} \right\} . \tag{3.2}$$

Here, $\varphi_B(r)$ is the in-plane projection of the *edgewise* curve in Figure 2.1, r is the actual blade radius, index Bi refers to blade number i and a_{ij} is denoted the mode weighting factor for blade number i in mode number j. The mode shapes are also illustrated in Figure 3.1.

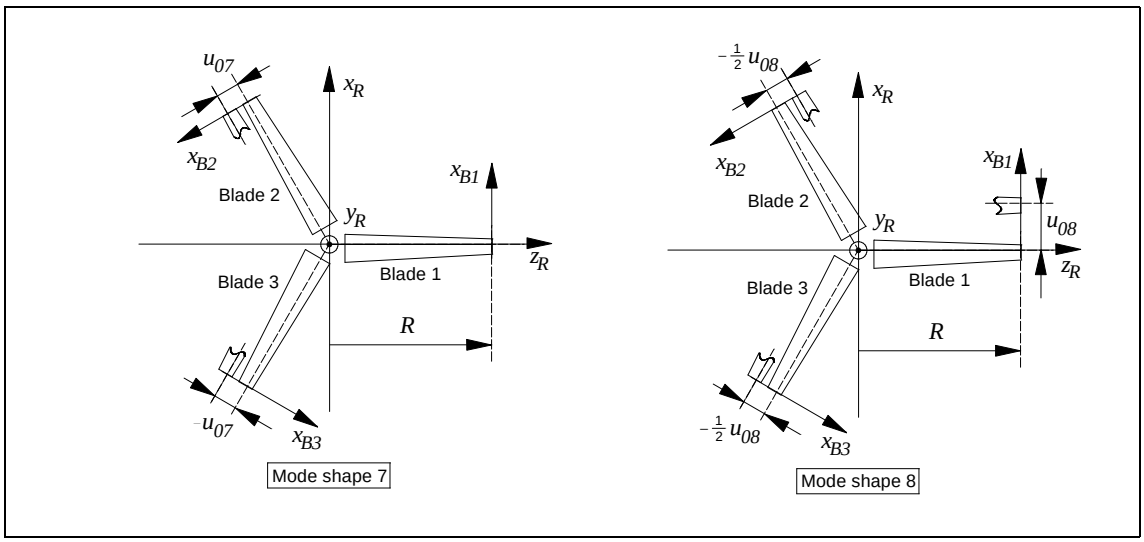

Figure 3.1. Relative tip deformations in the two basic edgewise mode shapes.

Vibration in the mode shapes are described by harmonic normal coordinates

$$\{q(t)\} = \left\{ \begin{array}{c} q_7(t) \\ q_8(t) \end{array} \right\} = \left\{ \begin{array}{c} u_{07} \sin(\omega_e t + \gamma_7) \\ u_{08} \sin(\omega_e t + \gamma_8) \end{array} \right\} , \tag{3.3}$$

where ω_e is the edgewise blade frequency, t is the time and the phases of the modes are denoted γ_7 and γ_8, respectively.

These normal coordinates result in the blade deformations

$$\{u(r,t)\} = \left\{ \begin{array}{c} u_{B1x} \\ u_{B2x} \\ u_{B3x} \end{array} \right\} = \left[\begin{array}{cc} \{\varphi_7(r)\} & \{\varphi_8(r)\} \end{array} \right] \left\{ \begin{array}{c} q_7(t) \\ q_8(t) \end{array} \right\} = [\varphi] \left\{ \begin{array}{c} q_7(t) \\ q_8(t) \end{array} \right\} , \tag{3.4}$$

which implicitly defines the modal matrix $[\varphi]$.

Using the actually chosen parameter values from Table 3.1 results in the blade tip deflections shown in Figure 3.2, covering one period of the edgewise vibration.

Table 3.1. Parameter values for presented examples.

Parameter	Actual value
u_{07}	$\frac{\sqrt{2}}{1}$ m = 1.4142 m
u_{08}	$\frac{\sqrt{6}}{2}$ m = 1.2247 m
γ_7	0.0°
γ_8	45.0°
$\omega = \omega_e = \omega_{lw}$	3.0 Hz = 18.850 rad/sec
Ω	0.5 Hz = 3.142 rad/sec
$\varphi_B(R)$	0.2
m_B	48.2 kg

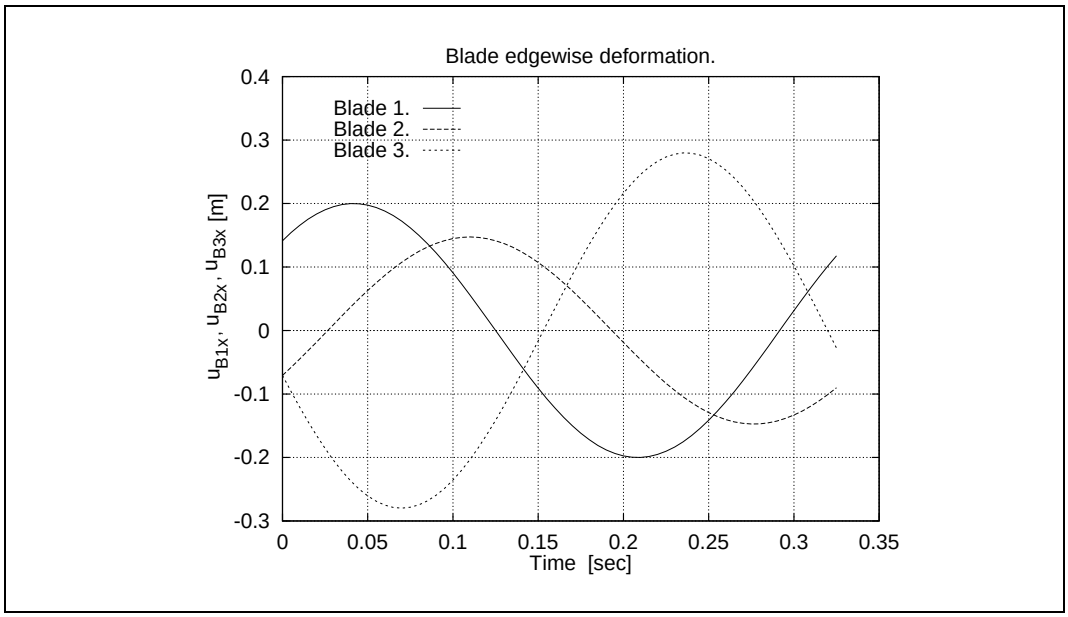

Figure 3.2. Blade tip deformations in edgewise direction.

As mentioned in Section 2.1 there is virtually no coupling between the edgewise blade modes and the shaft torsion, as the blades – according to the mode definitions in Equations 3.1 and 3.2 – are obviously dynamically in balance with respect to moment from the inertia force about an axis through the rotor center perpendicular to the rotor plane.

However, the resulting inertia force in the rotor plane is not zero, and a harmonic varying in-plane force is transferred to the main shaft. This force can interact with the global rotor whirl modes, i.e. exchange energy with these modes.

To illustrate this situation, the mass distribution along the blade is considered as well. The in-plane force due to vibration in the rotor plane arising from the associated inertia force is derived with reference to Figure 3.3.

In the local blade coordinate systems (x_{Bi}, y_{Bi}, z_{Bi}) only the force perpendicular to the blade axis is considered, i.e. the force in the x_{Bi}-direction. The mass, dm, of an infinitesimal radial blade length, dr, is considered

$$\mathrm{d}m = m(r)\mathrm{d}r \ , \tag{3.5}$$

where $m(r)$ is the mass per unit length of the blade, shown in Figure 2.1.

According to d'Alembert's principle, the infinitesimal inertia force yields

$$\mathrm{d}F_{ij}^{x_B}(r,t) = \varphi_B(r) a_{ij} \omega_e^2 u_{0j} \sin(\omega_e t + \gamma_j) m(r) \mathrm{d}r \ , \tag{3.6}$$

where the index i refers to the blade number, and j refers to the mode. The a_{ij} terms are the factors from the right side of Equations 3.1 and 3.2.

Assuming small in-plane rotations along the blade, the transformations of the local inertia force to the rotor coordinates can be linearized corresponding to assuming that the inertia force is perpendicular to the blade axis also in the deformed state. This means that the inertia force can be integrated along the blade and transformed afterwards.

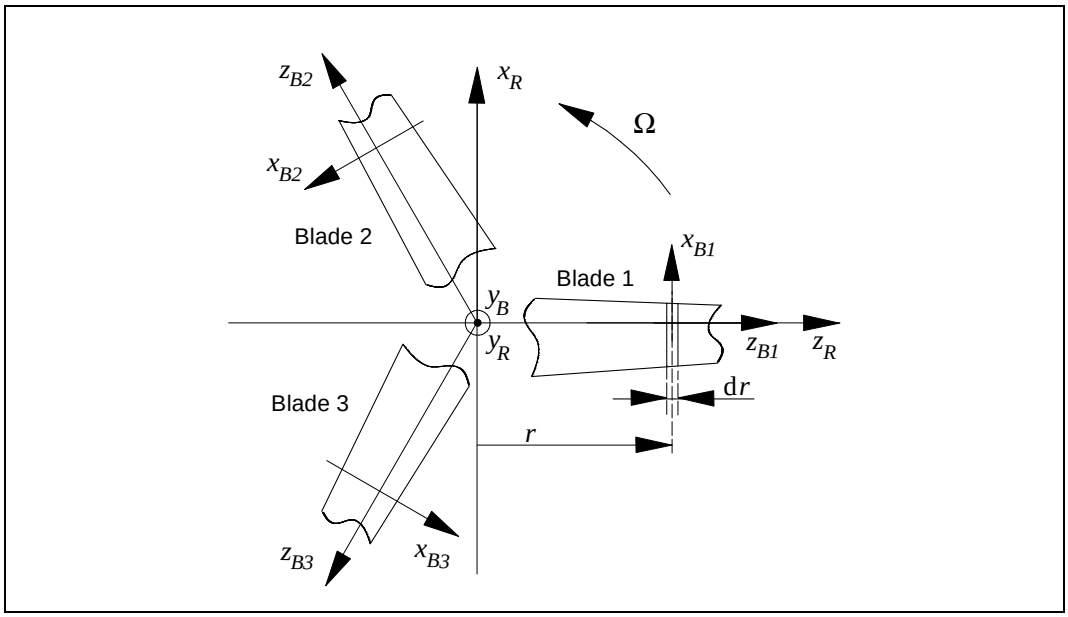

Figure 3.3. Coordinate systems involved in calculation of the resulting in-plane inertia force due to pure edgewise vibration.

The integrated inertia force in the x_{Bi}-direction yields

$$\begin{aligned} F_{ij}^{xB}(t) &= \left[\int_0^R \varphi_B(r)m(r)\mathrm{d}r\right] a_{ij}\omega_e^2 u_{0j}\sin(\omega_e t+\gamma_j) \\ &= m_B a_{ij}\omega_e^2 u_{0j}\sin(\omega_e t+\gamma_j)\,, \end{aligned} \tag{3.7}$$

which defines the mass

$$m_B = \int_0^R \varphi_B(r)m(r)\mathrm{d}r\ . \tag{3.8}$$

The transformation matrices transforming vectors from local blade coordinates, (x_{Bi}, y_{Bi}, z_{Bi}), to the rotor coordinates, (x_R, y_R, z_R), are

$$[T_{B1R}] = \begin{bmatrix} 1 & 0 & 0 \\ 0 & 1 & 0 \\ 0 & 0 & 1 \end{bmatrix}\ , \tag{3.9}$$

$$[T_{B2R}] = \begin{bmatrix} -\frac{1}{2} & 0 & \frac{\sqrt{3}}{2} \\ 0 & 1 & 0 \\ -\frac{\sqrt{3}}{2} & 0 & -\frac{1}{2} \end{bmatrix} \quad \text{and} \tag{3.10}$$

$$[T_{B3R}] = \begin{bmatrix} -\frac{1}{2} & 0 & -\frac{\sqrt{3}}{2} \\ 0 & 1 & 0 \\ \frac{\sqrt{3}}{2} & 0 & -\frac{1}{2} \end{bmatrix}\ . \tag{3.11}$$

Selecting only the terms from these transformation matrices, which influence the x_B-components, the transformations from all three blades are collected in one transformation

equation considering only the in-plane force components

$$\left\{ \begin{array}{c} F_{xj}^R \\ F_{zj}^R \end{array} \right\} = \left[\begin{array}{ccc} 1 & -\frac{1}{2} & -\frac{1}{2} \\ 0 & -\frac{\sqrt{3}}{2} & \frac{\sqrt{3}}{2} \end{array} \right] \left\{ \begin{array}{c} a_{1j} \\ a_{2j} \\ a_{3j} \end{array} \right\} m_B \omega_e^2 u_{0j} \sin(\omega_e t + \gamma_j) \; . \tag{3.12}$$

Inserting the a_{ij}-values for the two modes gives the in-plane force components. For mode 7 we get

$$\left\{ \begin{array}{c} F_{x7}^R \\ F_{z7}^R \end{array} \right\} = \left\{ \begin{array}{c} 0 \\ -\frac{\sqrt{3}}{2} \end{array} \right\} m_B \omega_e^2 u_{07} \sin(\omega_e t + \gamma_7) \; , \tag{3.13}$$

and for mode 8

$$\left\{ \begin{array}{c} F_{x8}^R \\ F_{z8}^R \end{array} \right\} = \left\{ \begin{array}{c} \frac{\sqrt{3}}{2} \\ 0 \end{array} \right\} m_B \omega_e^2 u_{08} \sin(\omega_e t + \gamma_8) \; , \tag{3.14}$$

and combined

$$\left\{ \begin{array}{c} F_x^R \\ F_z^R \end{array} \right\} = \frac{\sqrt{3}}{2} m_B \omega_e^2 \left\{ \begin{array}{c} u_{08} \sin(\omega_e t + \gamma_8) \\ -u_{07} \sin(\omega_e t + \gamma_7) \end{array} \right\} \; . \tag{3.15}$$

Basically, this force describes an elliptical orbit in the co-rotating coordinates, which might collapse to a straight line if the phase angles are numerically equal. Using the values from Table 3.1 we get the result presented in Figure 3.4. The force, indicated by the filled arrow, rotates in the same direction as the rotor – as illustrated by the non-filled arrows in the plot – with the frequency ω_e, which we also denote the *local blade whirl frequency*, ω_{lw}.

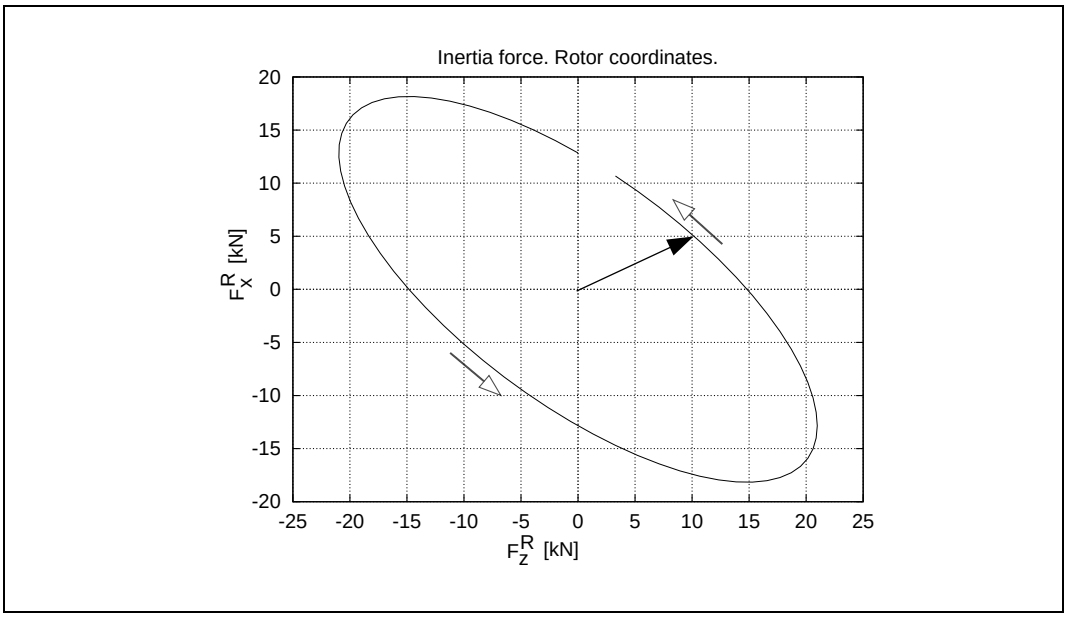

Figure 3.4. In-plane inertia force in rotating coordinates. The non-filled arrows indicate the rotation direction of the force.

Transformation to stationary tower coordinates is obtained by the following transformation matrices, covering either 3 or 2 dimensions:

$$[T_{RT}] = \begin{bmatrix} \cos(\Omega t) & 0 & \sin(\Omega t) \\ 0 & 1 & 0 \\ -\sin(\Omega t) & 0 & \cos(\Omega t) \end{bmatrix} \quad , \quad [T_{RT}^{xz}] = \begin{bmatrix} \cos(\Omega t) & \sin(\Omega t) \\ -\sin(\Omega t) & \cos(\Omega t) \end{bmatrix} , \tag{3.16}$$

which have been derived according to the definitions in Figure 3.6. Neglecting the y_T-component, which is zero, i.e. using the right matrix from Equation 3.16, the transformation results in the force vector in stationary coordinates

$$\begin{aligned} \begin{Bmatrix} F_x^T \\ F_z^T \end{Bmatrix} &= \frac{\sqrt{3}}{2} m_B \omega_e^2 \begin{bmatrix} \cos(\Omega t) & \sin(\Omega t) \\ -\sin(\Omega t) & \cos(\Omega t) \end{bmatrix} \begin{Bmatrix} u_{08} \sin(\omega_e t + \gamma_8) \\ -u_{07} \sin(\omega_e t + \gamma_7) \end{Bmatrix} \\ &= \frac{\sqrt{3}}{4} m_B \omega_e^2 \left\{ \begin{array}{c} \Big(-u_{07} \left[\cos((\omega_e - \Omega)t + \gamma_7) - \cos((\omega_e + \Omega)t + \gamma_7) \right] \\ \quad + u_{08} \left[\sin((\omega_e - \Omega)t + \gamma_8) - \sin((\omega_e + \Omega)t + \gamma_8) \right] \Big) \\ \Big(-u_{07} \left[\sin((\omega_e - \Omega)t + \gamma_7) - \sin((\omega_e + \Omega)t + \gamma_7) \right] \\ \quad - u_{08} \left[\cos((\omega_e - \Omega)t + \gamma_8) - \cos((\omega_e + \Omega)t + \gamma_8) \right] \Big) \end{array} \right\} . \end{aligned} \tag{3.17}$$

This result shows that the edgewise frequency is experienced as two in the stationary coordinates, namely $\omega_e \pm \Omega$. Using the parameter values from Table 3.1 gives the rotating force in stationary coordinates corresponding to Equation 3.17 as shown in Figure 3.5 by the filled arrow. The left plot in the figure shows one complete cycle of the edgewise vibration, and the right plot covers one complete rotor revolution. The non-filled arrows in the figures show the rotation direction of the force.

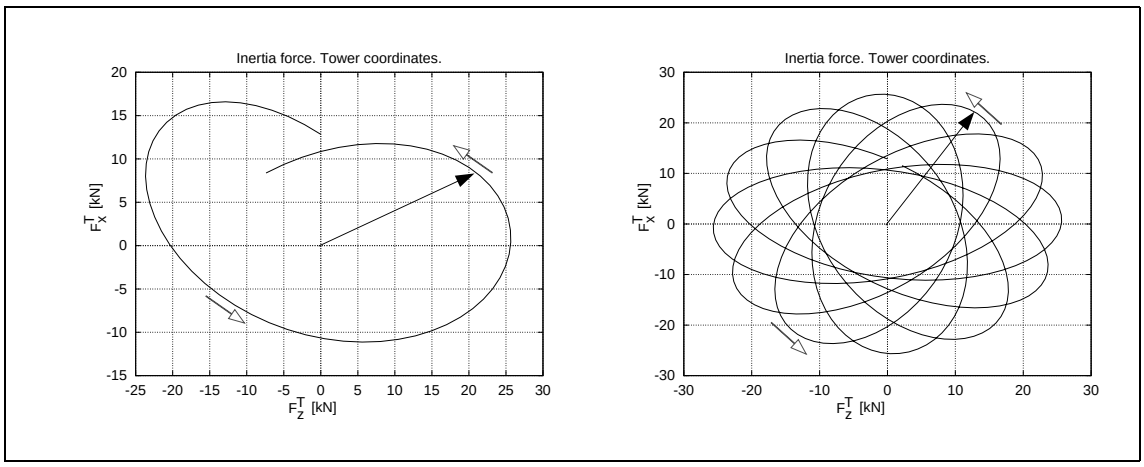

Figure 3.5. In-plane inertia force in stationary coordinates due to deformation in edgewise mode shapes. The left plot covers one period of the edgewise vibration, and the right plot covers one complete rotor revolution. The non-filled arrows show the rotation direction of the force.

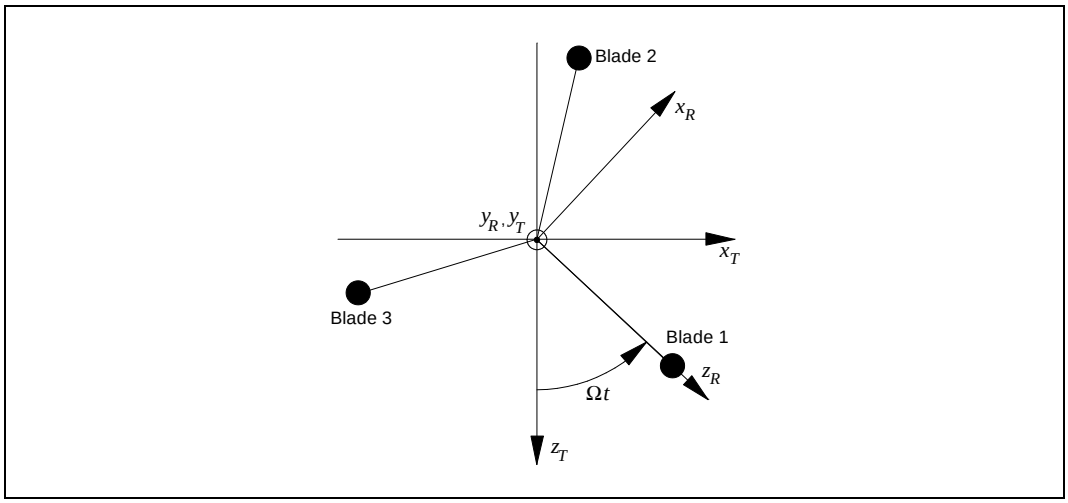

Figure 3.6. Rotating (R) and stationary (T) coordinate systems.

3.2 Decomposing elliptical orbits in circular orbits

The in-plane inertia force shown in Figure 3.4 describes an elliptical orbit in the (x_R, z_R)-plane. The force vector can be composed of two counter-rotating vectors with constant size. The two vectors may have either

- different size, which gives the elliptical orbit,
- same size, which degenerates the ellipse to a straight line, or
- one of the counter-rotating vectors may be zero, which gives a circular orbit.

In the present section we show the decomposition of the force vector in such two vectors, and further we derive the associated components of the blade modes. The purpose is to provide a description that in some aspects supports the understanding of the phenomena, and the decomposition may for instance be useful, when measurements are analyzed.

The parameters and the variables generally used for description of an ellipse are shown in the left plot in Figure 3.7. In the figure the resulting in-plane force is denoted $\{F_i\}$, the major semi-axis is denoted a and the minor semi-axis is denoted b. The angle from the z_R-axis to the major semi-axis is γ, and the angle from the z_R-axis to the rotating vector is $\omega_e t + \gamma_a$. The elliptical orbit can also be considered to be composed of two circular orbits – one corresponding to a vector with forward or progressive rotation, $\{F_p\}$, and the other corresponding to a vector with backward or retrograde rotation, $\{F_r\}$, as shown in the right plot in Figure 3.7.

The following relations are valid for these descriptions of the ellipses

$$F_p = |\{F_p\}| \;\; ; \;\; F_r = |\{F_r\}| \;\; ; \;\; \text{(vector size)} \tag{3.18}$$

$$a = F_p + F_r \;\; ; \;\; b = F_p - F_r \;\; ; \tag{3.19}$$

$$\gamma = \frac{1}{2}\left(\gamma_{Fp} - \gamma_{Fr}\right) \;\; ; \tag{3.20}$$

$$\gamma a = \gamma_{Fp} \; . \tag{3.21}$$

The resulting vector rotation is progressive, when $F_p > F_r$ and retrograde, when $F_r > F_p$.

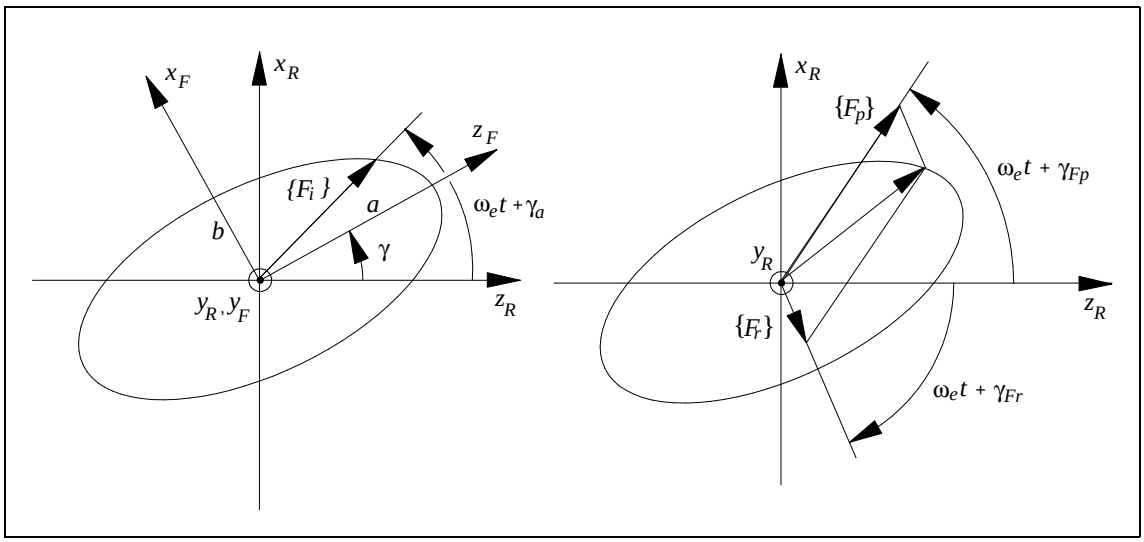

Figure 3.7. Orbits of in-plane inertia force in rotating coordinates.

The projection of the two circular orbits on the (x_R, z_R)-axis gives the in-plane force vector expressed by the progressive and retrograde components

$$\left\{ \begin{array}{c} F_x^R \\ F_z^R \end{array} \right\} = \left[\begin{array}{cc} \sin(\omega_e t + \gamma_{Fp}) & -\sin(\omega_e t + \gamma_{Fr}) \\ \cos(\omega_e t + \gamma_{Fp}) & \cos(\omega_e t + \gamma_{Fr}) \end{array} \right] \left\{ \begin{array}{c} F_p \\ F_r \end{array} \right\} . \tag{3.22}$$

By combination of Equations 3.15 and 3.22, the progressive and the retrograde components can be expressed by the amplitudes and the phases of the basic edgewise mode shapes. Equating coefficients to $\sin(\omega_e t)$ and $\cos(\omega_e t)$ terms yields the following four equations with four unknowns, F_p, F_r, γ_{Fp} and γ_{Fr}:

$$\left. \begin{array}{rcl} F_p \cos(\gamma_{Fp}) + F_r \cos(\gamma_{Fr}) & = & -\frac{\sqrt{3}}{2} m_B \omega_e^2 u_{07} \sin(\gamma_7) \\ F_p \sin(\gamma_{Fp}) + F_r \sin(\gamma_{Fr}) & = & \frac{\sqrt{3}}{2} m_B \omega_e^2 u_{07} \cos(\gamma_7) \\ F_p \sin(\gamma_{Fp}) - F_r \sin(\gamma_{Fr}) & = & \frac{\sqrt{3}}{2} m_B \omega_e^2 u_{08} \sin(\gamma_8) \\ F_p \cos(\gamma_{Fp}) - F_r \cos(\gamma_{Fr}) & = & \frac{\sqrt{3}}{2} m_B \omega_e^2 u_{08} \cos(\gamma_8) \end{array} \right\} , \tag{3.23}$$

giving the solutions

$$F_p = \frac{\sqrt{3}}{4} m_B \omega_e^2 \sqrt{u_{07}^2 + u_{08}^2 + 2 u_{07} u_{08} \sin(\gamma_8 - \gamma_7)} , \tag{3.24}$$

$$F_r = \frac{\sqrt{3}}{4} m_B \omega_e^2 \sqrt{u_{07}^2 + u_{08}^2 - 2 u_{07} u_{08} \sin(\gamma_8 - \gamma_7)} , \tag{3.25}$$

$$\gamma_{Fp} = \arctan \left[\frac{u_{07} \cos\gamma_7 + u_{08} \sin\gamma_8}{-u_{07} \sin\gamma_7 + u_{08} \cos\gamma_8} \right] \text{ and} \tag{3.26}$$

$$\gamma_{Fr} = \arctan \left[\frac{u_{07} \cos\gamma_7 - u_{08} \sin\gamma_8}{-u_{07} \sin\gamma_7 - u_{08} \cos\gamma_8} \right] . \tag{3.27}$$

Transforming the in-plane force from Equation 3.22 to stationary T-coordinates yields

$$\begin{Bmatrix} F_x^T \\ F_z^T \end{Bmatrix} = [T_{RT}^{xz}] \begin{Bmatrix} F_x^R \\ F_z^R \end{Bmatrix}$$
$$= \begin{bmatrix} \sin\left[(\omega_e + \Omega)\, t + \gamma_{Fp}\right] & -\sin\left[(\omega_e - \Omega)\, t + \gamma_{Fr}\right] \\ \cos\left[(\omega_e + \Omega)\, t + \gamma_{Fp}\right] & \cos\left[(\omega_e - \Omega)\, t + \gamma_{Fr}\right] \end{bmatrix} \begin{Bmatrix} F_p \\ F_r \end{Bmatrix}. \quad (3.28)$$

By use of the example data from Table 3.1 the progressive and the retrograde circular components are calculated and shown in Figure 3.8.

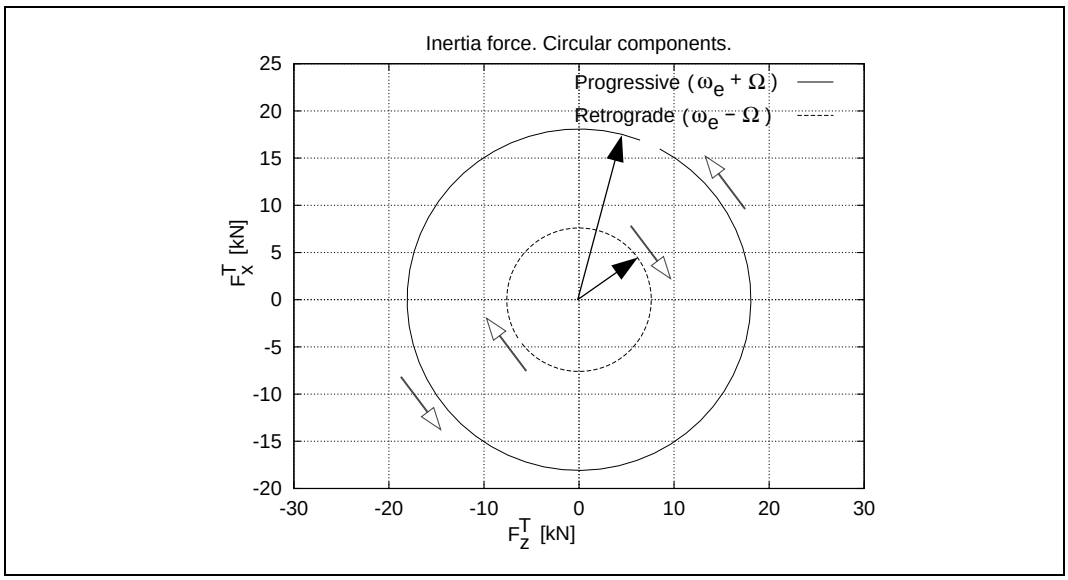

Figure 3.8. Forward (progressive) and backward (retrograde) whirl components of the in-plane inertia force. The plot axes refer to the T-coordinates. The appearance of the components in R-coordinates is the same, but referenced to these coordinates the frequency of both components is $\omega_e = \omega_{lw}$, the local blade whirl frequency.

Accordingly, the blade deformations corresponding to progressive and retrograde in-plane forces, respectively, can be found by resolving each of them with respect to the basic mode shapes, $\{\varphi_7\}$ and $\{\varphi_8\}$.

Pure progressive in-plane force is obtained with the same amplitude of the two modes, u_p, and a phase difference of $\gamma_{8p} - \gamma_{7p} = \frac{\pi}{2}$, which can be observed from Equations 3.24 and 3.25. Correspondingly, pure retrograde in-plane force is obtained by the common mode amplitude u_r, and phase difference $\gamma_{8r} - \gamma_{7r} = -\frac{\pi}{2}$.

The constant phase difference implies that only one phase is needed for description of each rotation direction. We choose $\gamma_{7p} = \gamma_{up}$ and $\gamma_{7r} = \gamma_{ur}$ in the derivations below.

The corresponding harmonic normal coordinates are found from Equation 3.3. The progressive coordinates are expressed by

$$\{q_p(t)\} = \begin{Bmatrix} q_{7p}(t) \\ q_{8p}(t) \end{Bmatrix} = \begin{Bmatrix} u_p \sin(\omega_e t + \gamma_{up}) \\ u_p \cos(\omega_e t + \gamma_{up}) \end{Bmatrix}, \quad (3.29)$$

and the retrograde coordinates by

$$\{q_r(t)\} = \left\{ \begin{array}{c} q_{7r}(t) \\ q_{8r}(t) \end{array} \right\} = \left\{ \begin{array}{c} u_r \sin(\omega t + \gamma_{ur}) \\ u_r \cos(\omega t + \gamma_{ur}) \end{array} \right\} . \tag{3.30}$$

The total blade deformations are obtained by combining these equations, which yields

$$\begin{aligned} \{u(r,t)\} &= \left[\begin{array}{cc} \varphi_7(r) & \varphi_8(r) \end{array} \right] \Big(\{q_p(t)\} + \{q_r(t)\} \Big) \\ &= \left[\begin{array}{cc} \varphi_7(r) & \varphi_8(r) \end{array} \right] \left\{ \begin{array}{c} u_p \sin(\omega_e t + \gamma_{up}) + u_r \sin(\omega_e t + \gamma_{ur}) \\ u_p \cos(\omega_e t + \gamma_{up}) - u_r \cos(\omega_e t + \gamma_{ur}) \end{array} \right\} . \end{aligned} \tag{3.31}$$

Equating the coefficients to the $\sin(\omega_e t)$ and the $\cos(\omega_e t)$ terms from Equations 3.3, 3.4 and 3.31 yields the following four equations with four unknowns, u_p, u_r, γ_{up} and γ_{ur}, equivalent to Equations 3.23:

$$\left. \begin{array}{rcr} u_p \sin(\gamma_{up}) + u_r \sin(\gamma_{ur}) &=& u_{07} \sin(\gamma_7) \\ u_p \cos(\gamma_{up}) + u_r \cos(\gamma_{ur}) &=& u_{07} \cos(\gamma_7) \\ u_p \cos(\gamma_{up}) - u_r \cos(\gamma_{ur}) &=& u_{08} \sin(\gamma_8) \\ u_p \sin(\gamma_{up}) - u_r \sin(\gamma_{ur}) &=& -u_{08} \cos(\gamma_8) \end{array} \right\} , \tag{3.32}$$

giving the solutions

$$u_p = \frac{1}{2} \sqrt{u_{07}^2 + u_{08}^2 + 2u_{07}u_{08} \sin(\gamma_8 - \gamma_7)} , \tag{3.33}$$

$$u_r = \frac{1}{2} \sqrt{u_{07}^2 + u_{08}^2 - 2u_{07}u_{08} \sin(\gamma_8 - \gamma_7)} , \tag{3.34}$$

$$\gamma_{up} = \arctan \left[\frac{u_{07} \sin\gamma_7 - u_{08} \cos\gamma_8}{u_{07} \cos\gamma_7 + u_{08} \sin\gamma_8} \right] \text{ and} \tag{3.35}$$

$$\gamma_{ur} = \arctan \left[\frac{u_{07} \sin\gamma_7 + u_{08} \cos\gamma_8}{u_{07} \cos\gamma_7 - u_{08} \sin\gamma_8} \right] . \tag{3.36}$$

It is observed that the rotating force components from Equations 3.24 and 3.25 can be expressed by the progressive and the retrograde mode amplitudes

$$F_p = \frac{\sqrt{3}}{2} m_B \omega_e^2 u_p \text{ and} \tag{3.37}$$

$$F_r = \frac{\sqrt{3}}{2} m_B \omega_e^2 u_r . \tag{3.38}$$

Considering the deformations corresponding to progressive and retrograde resolutions separately shows that the blades are vibrating with the same amplitudes, but with different phases.

From Equation 3.31 the following is obtained by rewriting the trigonometric functions and inserting the mode shape components from Equations 3.1 and 3.2

$$\{u_p\} = u_p \varphi_B(r) \sqrt{\frac{3}{2}} \left\{ \begin{array}{c} \cos(\omega_e t + \gamma_{up}) \\ \cos(\omega_e t + \gamma_{up} + \frac{4\pi}{3}) \\ \cos(\omega_e t + \gamma_{up} + \frac{2\pi}{3}) \end{array} \right\} \text{ and} \tag{3.39}$$

$$\{u_r\} = u_r \varphi_B(r)(-\sqrt{\frac{3}{2}}) \left\{ \begin{array}{c} \cos(\omega_e t + \gamma_{ur}) \\ \cos(\omega_e t + \gamma_{ur} + \frac{2\pi}{3}) \\ \cos(\omega_e t + \gamma_{ur} + \frac{4\pi}{3}) \end{array} \right\} . \tag{3.40}$$

We denote these blade deformations *local blade whirl*, and refer them to the rotation direction as *forward* and *backward* (or alternatively *progressive* and *retrograde*), respectively.

By use of the example data from Table 3.1 the progressive and the retrograde deformation components are calculated and shown in Figure 3.9.

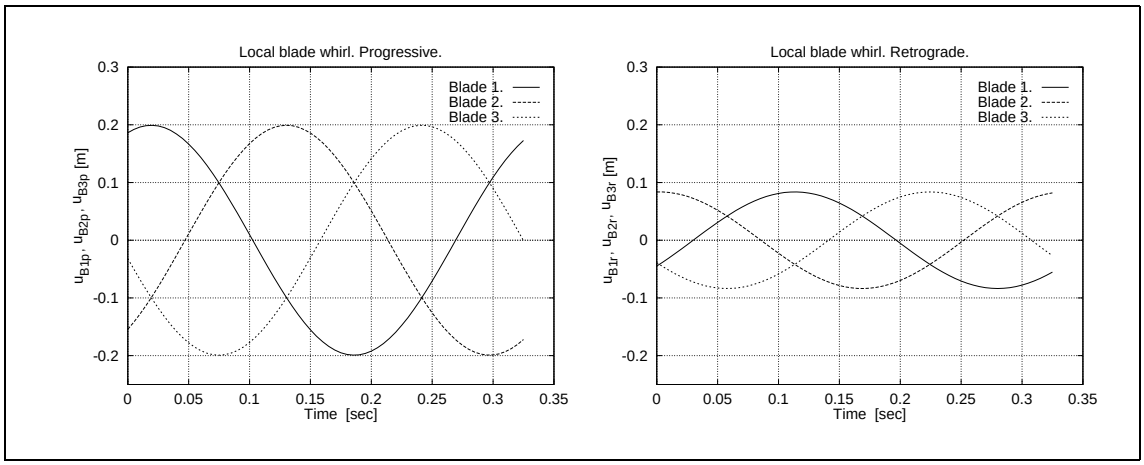

Figure 3.9. Progressive and retrograde components of edgewise blade deformations.

3.3 Decomposing the blade response for an operating turbine

In the previous example we assumed that the normal coordinates were known. If we, on the other hand, know the edgewise blade response for all three blades – either as deformations or as moments – we are able to determine the normal coordinates corresponding to this response approximately and subsequently to apply the decomposition presented above. The principle is outlined below, and an example for a turbine operating in free wind is presented. The response for an operating turbine is varying due to the time varying loads, and the *local blade whirl components* are time varying, accordingly.

Assuming that the fundamental edgewise mode shapes dominate the response, the blade deformation in the edgewise direction can be determined from the deformation in one radial blade station – say at the tip, i.e. at radius $r = R$, meaning that $\{u(R,t)\}$ is known – or from the moment – say the moment at the blade root, $\{M_{B0}(t)\}$ – assuming that the moment is proportional to the deformation

$$\{M_{B0}\} = \left\{ \begin{array}{c} M_{B10}(t) \\ M_{B20}(t) \\ M_{B30}(t) \end{array} \right\} = K_{uM} \{u_R(R,t)\} = K_{uM} \left\{ \begin{array}{c} u_{B1x}(R,t) \\ u_{B2x}(R,t) \\ u_{B3x}(R,t) \end{array} \right\} , \tag{3.41}$$

where K_{uM} is the proportionality factor equivalent to a stiffness with dimension [Nm/m].

As the edgewise deformations are influenced by the aerodynamic driving force and the 1P gravity force, we choose to remove the mean deformation and the harmonic 1P deformation per rotor revolution.

The total response is expressed as the sum

$$\{u_R(R,t)\} = \{u_m(R)\} + \{u_{1P}(R,t)\} + \{u_e(R,t)\} \ , \tag{3.42}$$

where

$\{u_m(R)\}$ is the mean deformation calculated over one complete revolution,

$\{u_{1P}(R,t)\}$ is the deformation due to the gravity force and the 1P aero-force and

$\{u_e(R,t)\}$ is the deformation due to the vibration in the fundamental edgewise mode shape and the higher order modes.

When the fundamental edgewise mode shapes dominate $\{u_e\}$, this vector can be resolved in its components with good approximation according to the theory presented in the previous Sections 3.1 and 3.2.

Calculation for one complete rotor revolution gives the mean

$$\{u_m(R)\} = \frac{1}{T_P}\int_0^{T_P} \{u_R(R,t)\}\,\mathrm{d}t \ , \tag{3.43}$$

where $T_P = \frac{2\pi}{\Omega}$ is the period for one revolution.

Correspondingly, the 1P contribution is expressed by the truncated Fourier series

$$\{u_{1P}(R,t)\} = \left[\left\{ \begin{array}{c} a_1 \\ a_2 \\ a_3 \end{array} \right\} \cos(\Omega t) + \left\{ \begin{array}{c} b_1 \\ b_2 \\ b_3 \end{array} \right\} \sin(\Omega t) \right] \ , \tag{3.44}$$

where the coefficients are calculated from

$$\left\{ \begin{array}{c} a_1 \\ a_2 \\ a_3 \end{array} \right\} = \frac{2}{T_P}\int_0^{T_P} \{u_R(R,t)\}\cos(\Omega t)\mathrm{d}t \tag{3.45}$$

and

$$\left\{ \begin{array}{c} b_1 \\ b_2 \\ b_3 \end{array} \right\} = \frac{2}{T_P}\int_0^{T_P} \{u_R(R,t)\}\sin(\Omega t)\mathrm{d}t \ . \tag{3.46}$$

Having determined the mean and the 1P component, the remainder of the response, which we expect to be dominated by the vibration in the fundamental edgewise mode shapes, can be found from

$$\{u_e(R,t)\} = \{u_R(R,t)\} - \{u_m(R)\} - \{u_{1P}(R,t)\} \ , \tag{3.47}$$

which we expand in the modal components according to Equation 3.4

$$\{u_e(R,t)\} = \left\{ \begin{array}{c} u_{B1x}(R,t) \\ u_{B2x}(R,t) \\ u_{B3x}(R,t) \end{array} \right\} = \left[\begin{array}{cc} \{\varphi_7(R)\} & \{\varphi_8(R)\} \end{array} \right] \left\{ \begin{array}{c} q_7(t) \\ q_8(t) \end{array} \right\} \ . \tag{3.48}$$

Solving for the normal coordinates we get

$$\left\{ \begin{array}{c} q_7(t) \\ q_8(t) \end{array} \right\} = \frac{1}{\varphi_B^2(R)} \left[\begin{array}{c} \{\varphi_7(R)\}^T \\ \{\varphi_8(R)\}^T \end{array} \right] \{u_e(R,t)\} \ , \tag{3.49}$$

where T denotes transposition, and the modal vectors are the rows of the transposed modal matrix, $[\varphi]^T$.

Now, the theory from the previous Sections 3.1 and 3.2 can be used for decomposition and analysis. Examples are presented in Section 5.

4 Global rotor whirl

The investigation of stall induced edgewise blade vibrations for a three bladed wind turbine reveals that the coupled modes of the turbine might be of great importance for developing and sustaining the vibrations. During the vibration the local rotor modes, which involve the two basic edgewise blade bending modes described in Section 2.1 for a three bladed turbine as modes 7 and 8, give rise to an in-plane harmonic inertia force with the blade edgewise natural frequency, ω_e. This force might interact with the global rotor whirl modes. To provide a better basis for understanding this phenomenon the global rotor whirl modes are described in the present section by use of a simple wind turbine model [5] with only four degrees of freedom (DOFs) roughly corresponding to tilt and yaw rotations at the tower top and at the main bearing. In this model the shaft, the hub and the blades are considered infinitely stiff, and the rotor moves as a rigid body. For a real turbine the flexibility of the shaft, the hub and the blades modify these modes significantly, but the simple model represents the basic behaviour of the global rotor whirl modes with good approximation.

The global rotor whirl modes are related to the 1^{st} and 2^{nd} rotor tilt and yaw modes as identified at stand still for the three bladed example turbine in Section 2.1 and listed in Table 2.1 as modes 4, 5, 9 and 10. The present simplified model aims at describing these modes and how they depend on the rotational speed of the rotor, Ω.

The simple 4-DOF model is illustrated in Figure 4.1.

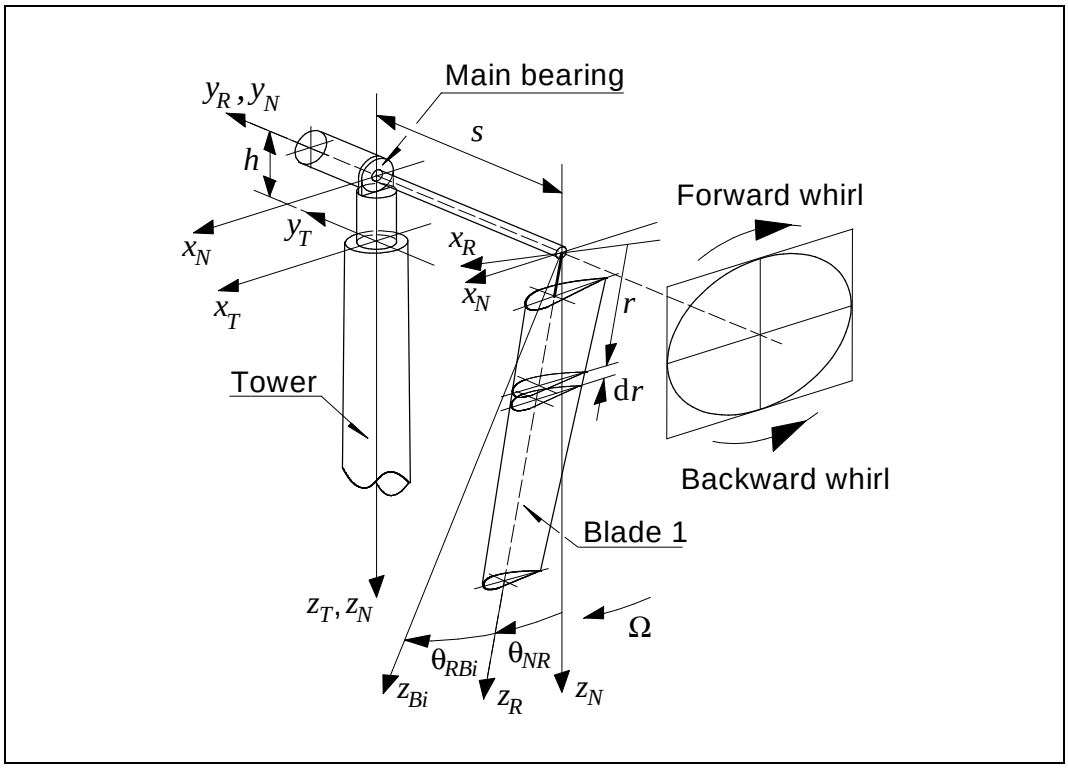

Figure 4.1. Simple 4-DOF model of wind turbine.

The model considers only the influence of the tower through the rotations in the tilt and the yaw directions at the tower top, i.e. the rotation θ_{xT} about the x_T-axis and the rotation θ_{zT} about the z_T-axis, respectively. A concentrated mass moment of inertia, I_T, representing the tower and the nacelle is assigned to these DOFs. The corresponding rotational stiffnesses

belonging to these DOFs are denoted k_{xT} and k_{zT}, respectively. The remaining two degrees of freedom represent the elastic rotations in the tilt and yaw directions of the main bearing, θ_{xN} and θ_{zN}, about the axes x_N and z_N, respectively. The corresponding rotational stiffnesses are denoted k_{xN} and k_{zN}, respectively. No concentrated mass moment of inertia is assigned to these bearing rotations, as the inertia is assumed small compared to the mass moment of inertia of the rotor. Thus, all the deformations take place in a stationary frame of reference, and the equations of motion can be derived without the periodic azimuthal dependency. This approximation might be rather rough for a real turbine, because the deformations of the shaft, the hub and the blades usually have a significant influence on the considered vibration modes. However, the model is well suited for the purpose of illustrating the basic behaviour of the global rotor whirl modes, which we have in mind.

The sign of the rotations are chosen according to a right-hand screw convention, meaning that the sign is positive, when the equivalent rotation of a right-hand screw moves it in the positive direction of the actual coordinate axis.

In summary, the model degrees of freedom are:

1. θ_{xT}, rotation about the tower top x_T-axis, corresponding to rotor tilt rotation.
2. θ_{zT}, rotation about the tower top z_T-axis, corresponding to rotor yaw rotation.
3. θ_{xN}, rotation about the bearing x_N-axis, corresponding to rotor tilt rotation.
4. θ_{zN}, rotation about the bearing z_N-axis, corresponding to rotor yaw rotation.

The deformations are assumed small, so that the rotations can be added as vectors, and the total rotations of the rotor y_R-axis, which coincides with the rotor shaft, become:

$$\theta_{xS} = \theta_{xT} + \theta_{xN} \tag{4.1}$$

and

$$\theta_{zS} = \theta_{zT} + \theta_{zN} \ . \tag{4.2}$$

This four DOF system has four natural frequencies, and the corresponding mode shapes are characterized by the phase of the rotations. For instance, the phase of the rotations for the two mode shapes, which involve tiltwise rotation, are

1. θ_{xT} and θ_{xN} in *phase* and
2. θ_{xT} and θ_{xN} in *counter-phase*.

The mode with the rotations in phase has the lower frequency of the two.

The next step in establishing the model is the derivation of the equations of motion for the turbine with the rotor rotating with constant angular velocity, Ω. The most important part of this task is the derivation of the inertia forces on the rotor, which finally provides us with the mass matrix and the gyroscopic matrix. We go through the details of this derivation. We apply Newton's method for calculation of the inertia force on an infinitesimal mass element at radius r on a blade, e.g. blade number i:

$$\mathrm{d}m = m\,(r, \theta_{RBi})\,\mathrm{d}r \ , \tag{4.3}$$

where

$m(r, \theta_{RBi})$ is the mass per unit length at radius r for blade number i and

θ_{RBi} is the angular position in the rotor plane of blade number i, measured from the z_R-axis of the (x_R, y_R, z_R)-coordinate system, which is fixed in the rotor, with the z_R-axis coinciding with the axis of blade 1, z_{B1}.

The mass element is shown in Figure 4.1.

The acceleration is derived as the second derivative with respect to time of the position vector to the mass element. Assuming that the distance between the origo of the T-coordinate system and the origo of the N-coordinate system – denoted h in Figure 4.1 – is zero, the position in stationary T-coordinates yields

$$\begin{aligned} \{r^T\} &= [T_{NT}] \left[\begin{Bmatrix} 0 \\ -s \\ 0 \end{Bmatrix} + [T_{RN}] \begin{Bmatrix} r\sin(\theta_{RBi}) \\ 0 \\ r\cos(\theta_{RBi}) \end{Bmatrix} \right] \\ &= [T_{NT}] \left[\{r_N^N\} + [T_{RN}] \{r_{Bi}^R\} \right] , \end{aligned} \tag{4.4}$$

which implicitly defines the local position vectors $\{r_N^N\}$ and $\{r_{Bi}^R\}$. The upper vector index identifies the actual coordinate system, to which the vector components are referenced, and the lower index is just a part of the vector name. In Equation 4.4 s is the horizontal distance from the center-line of the tower to the center of the rotor and

$$[T_{NT}] = \begin{bmatrix} 1 & -\theta_{zS} & 0 \\ \theta_{zS} & 1 & -\theta_{xS} \\ 0 & \theta_{xS} & 1 \end{bmatrix} \tag{4.5}$$

is a linearized transformation matrix, which transforms a vector from nacelle-coordinates (N) to tower-coordinates (T), and

$$[T_{RN}] = \begin{bmatrix} \cos(\theta_{NR}) & 0 & \sin(\theta_{NR}) \\ 0 & 1 & 0 \\ -\sin(\theta_{NR}) & 0 & \cos(\theta_{NR}) \end{bmatrix} \tag{4.6}$$

is a transformation matrix, which transforms a vector from rotor-coordinates (R) to nacelle-coordinates (N).

Differentiation of the position vector with respect to time – here expressed by the operator $\left[\frac{\mathrm{d}}{\mathrm{d}t}\right] = [\,\dot{}\,]$ – gives the velocity of the mass element

$$\begin{aligned} \{\dot{r}^T\} = [T_{NT}] \Big[\{\omega_{NT}^N\} \times \Big(\{r_N^N\} + [T_{RN}] \{r_{Bi}^R\} \Big) \\ + [T_{RN}] \Big(\{\omega_{RN}^R\} \Big) \Big] . \end{aligned} \tag{4.7}$$

After linearization the rotation vectors are derived to

$$\{\omega_{NT}^N\} \simeq \begin{Bmatrix} \dot{\theta}_{xT} + \dot{\theta}_{xN} \\ 0 \\ \dot{\theta}_{zT} + \dot{\theta}_{zN} \end{Bmatrix} \tag{4.8}$$

and

$$\{\omega_{RN}^R\} = \left\{ \begin{array}{c} 0 \\ \Omega \\ 0 \end{array} \right\} , \tag{4.9}$$

where Ω is the constant angular velocity of the rotor.

Finally, derivation of the velocity vector with respect to time yields the acceleration of the mass element. The acceleration is transformed to rotor coordinates (upper index R) merely to simplify the expression

$$\begin{aligned} \{\ddot{r}^R\} \;=\; & \Big([T_{NR}]\{\omega_{NT}^N\}\Big) \times \Big[\Big([T_{NR}]\{\omega_{NT}^N\}\Big) \times \Big([T_{NR}]\{r_N^N\} + \{r_{Bi}^R\}\Big) \\ & \qquad + 2\{\omega_{RN}^R\} \times \{r_{Bi}^R\}\Big] \\ & + \{\omega_{RN}^R\} \times \Big(\{\omega_{RN}^R\} \times \{r_{Bi}^R\}\Big) \\ & + \Big([T_{NR}]\{\dot{\omega}_{NT}^N\}\Big) \times \Big([T_{NR}]\{r_N^N\} + \{r_{Bi}^R\}\Big) , \end{aligned} \tag{4.10}$$

where $[T_{NR}]$ is the transposed of $[T_{RN}]$.

The moment from the inertia forces with respect to the rotation degrees of freedom are obtained by integration over the three blades. For example for the rotations in the tower coordinates (T) we get

$$\{M^T\} = \sum_{i=1}^{3} \left[\int_0^R \{r^T\} \times \Big(- [T_{NT}][T_{RN}]\{\ddot{r}^R\}\, m\,(r, \theta_{RBi})\Big) \mathrm{d}r \right] . \tag{4.11}$$

Finally, the linearized equations of motion are obtained by requiring moment equilibrium at each degree of freedom between inertia forces, elastic forces and external forces, resulting in the equation

$$[M]\left\{\ddot{\theta}\right\} + [C]\left\{\dot{\theta}\right\} + [K]\{\theta\} = \{F\} \tag{4.12}$$

with the mass matrix

$$[M] = \begin{bmatrix} I_T + I_R + s^2 M_R & 0 & I_R + s^2 M_R & 0 \\ 0 & I_T + I_R + s^2 M_R & 0 & I_R + s^2 M_R \\ I_R + s^2 M_R & 0 & I_R + s^2 M_R & 0 \\ 0 & I_R + s^2 M_R & 0 & I_R + s^2 M_R \end{bmatrix} , \tag{4.13}$$

the gyroscopic matrix

$$[C] = \begin{bmatrix} 0 & -\Omega J & 0 & -\Omega J \\ \Omega J & 0 & \Omega J & 0 \\ 0 & -\Omega J & 0 & -\Omega J \\ \Omega J & 0 & \Omega J & 0 \end{bmatrix} , \tag{4.14}$$

the stiffness matrix

$$[K] = \begin{bmatrix} k_{xT} & 0 & 0 & 0 \\ 0 & k_{zT} & 0 & 0 \\ 0 & 0 & k_{xN} & 0 \\ 0 & 0 & 0 & k_{zN} \end{bmatrix} , \tag{4.15}$$

the vector with the elastic angular deformations

$$\{\theta\} = \begin{Bmatrix} \theta_{xT} \\ \theta_{zT} \\ \theta_{xN} \\ \theta_{zN} \end{Bmatrix} \tag{4.16}$$

and the vector with moments resulting from external forces

$$\{F\} = \begin{Bmatrix} M_{xT} \\ M_{zT} \\ M_{xN} \\ M_{zN} \end{Bmatrix} , \tag{4.17}$$

where

I_R	is the mass moment of inertia of the rotor about an axis in the rotor plane, e.g. x_R,
$J = 2I_R$	is the mass moment of inertia of the rotor about an axis perpendicular to the rotor plane, i.e. y_R, and
M_R	is the total mass of the rotor.

Now, assuming that the solutions to Equation 4.12 are harmonic with angular frequency ω

$$\{\theta\} = \begin{Bmatrix} \theta_{xT0} \\ \theta_{zT0} \\ \theta_{xN0} \\ \theta_{zN0} \end{Bmatrix} \exp^{i\omega t} = \{\theta_0\} \exp^{i\omega t} \tag{4.18}$$

and that the external forces are zero, $\{F\} = \{0\}$, the natural frequencies are determined from the equation

$$\Big(-\omega^2 [M] + i\omega [C] + [K] \Big) \{\theta_0\} \exp^{i\omega t} = \{0\} , \tag{4.19}$$

where i is the imaginary unit.

The characteristic equation (the determinant of the matrix sum in the left parenthesis in Equation 4.19) is derived and the roots of this equation are found to give the natural frequencies, $\omega = \omega_n = \omega_{gw}$, which we identify as the *global rotor whirl* frequencies

$$\mathrm{Det}\Big(I_T, I_R, s^2 M_R, J, \Omega, k_{xT}, k_{zT}, k_{xN}, k_{zN}, \omega_n \Big) = 0 . \tag{4.20}$$

The determinant expression is rather complex (a polynomium with ω_n in the 8^{th} power) and the solutions are most conveniently found by numerical methods. If we assume that the

stiffnesses are symmetric, i.e. $k_{xT} = k_{zT} = k_T$ and $k_{xN} = k_{zN} = k_N$, we get the somewhat reduced determinant expression

$$\begin{aligned}
\mathrm{Det}(\omega_n) \quad = \quad & \Big[I_T(I_B + s^2 M_R)\omega_n^4 - I_T J\Omega\omega_n^3 \\
& - \Big(I_T k_N + \left(I_B + s^2 M_R\right)\left(k_T + k_N\right) \Big)\omega_n^2 \\
& + J\Omega\left(k_T + k_N\right)\omega_n + k_T k_N \Big] \times \\
& \Big[I_T(I_B + s^2 M_R)\omega_n^4 + I_T J\Omega\omega_n^3 \\
& - \Big(I_T k_N + \left(I_B + s^2 M_R\right)\left(k_T + k_N\right) \Big)\omega_n^2 \\
& - J\Omega\left(k_T + k_N\right)\omega_n + k_T k_N \Big] \, . \qquad (4.21)
\end{aligned}$$

4.1 Examples

Below we show examples of solution of the characteristic equation. We choose values for structural parameters typical for a wind turbine with 19 m blades. Two configurations are chosen with different stiffnesses in the rotational DOFs. The actual values of the structural parameters are listed in Table 4.1.

Table 4.1. Structural parameters for the example turbines.

Variable	Units	Example 1	Example 2
I_T	kgm^2	$2.5\,10^5$	$2.5\,10^5$
I_R	kgm^2	$1.9\,10^5$	$1.9\,10^5$
$s^2 M_R$	kgm^2	$4.3\,10^4$	$4.3\,10^4$
k_{xT}	Nm/rad	$1.6\,10^8$	$6.0\,10^7$
k_{zT}	Nm/rad	$0.70 \times k_{xT}$	$0.75 \times k_{xT}$
k_{xN}	Nm/rad	$1.4\,10^7$	$4.0\,10^7$
k_{zN}	Nm/rad	k_{xN}	k_{xN}

In Figure 4.2 the natural frequencies for Example 1 are shown as function of rotor speed. The two lowest frequencies correspond to the 1^{st} tilt-yaw mode shapes. It is observed that the natural frequencies depend considerably on the rotational speed, due to the gyroscopic forces. The yaw and tilt rotations are uncoupled at stand still, but when the turbine rotates, the two deformations couple due to the gyroscopic forces. The degree of coupling depends on how much the direction of the rotor shaft – the direction of the y_R-axis – is changed due to the elastic deformations. In general, the coupling results in deformations, which makes the rotor center follow an elliptical orbit as indicated in Figure 4.1. In the present context we denote this motion of the rotor *global rotor whirl*. The orbit is characterized by the direction in which the rotor center travels the elliptical path. Depending on the actual stiffnesses the direction might be either *forward* or *backward*. *Forward whirl* means that the elliptical orbit is travelled in the same direction as the turbine rotates, i.e. in the same direction as Ω, and vice versa for *backward whirl*. The actual directions for the example are indicated in Figure 4.2. The direction of the whirl motion has been found by solving the equations of motion in the time domain by applying a harmonic excitation at the actual natural frequency, as demonstrated in Section 7.

The two highest frequencies for Example 1 correspond to the 2^{nd} tilt-yaw mode shapes. In the present case they depend only very little on the rotor speed, which means that the deformations at the tower top and at the main bearing are almost identical, but in counter-phase, so that the direction of the rotor shaft is practically unchanged during the vibration.

The natural frequencies for Example 2 are shown in Figure 4.3. The changed stiffnesses make the 1^{st} tilt-yaw modes less dependent on the rotor speed, while the 2^{nd} tilt-yaw modes are now more influenced by the rotor speed, when compared to Example 1.

The global whirl frequencies might be found for an actual wind turbine by an aeroelastic code without introducing simplifications, e.g. by carrying out simulations with harmonic forces or moments, which are chosen with size, frequencies and orientation, so that the whirl modes are excited. The frequencies might be guessed by some trial and error process, and frequency bands can be investigated by letting the excitation frequency vary slowly during the simulation period. Examples of excitation and identification of the global whirl modes by use of a general aeroelastic code are presented in Section 7.

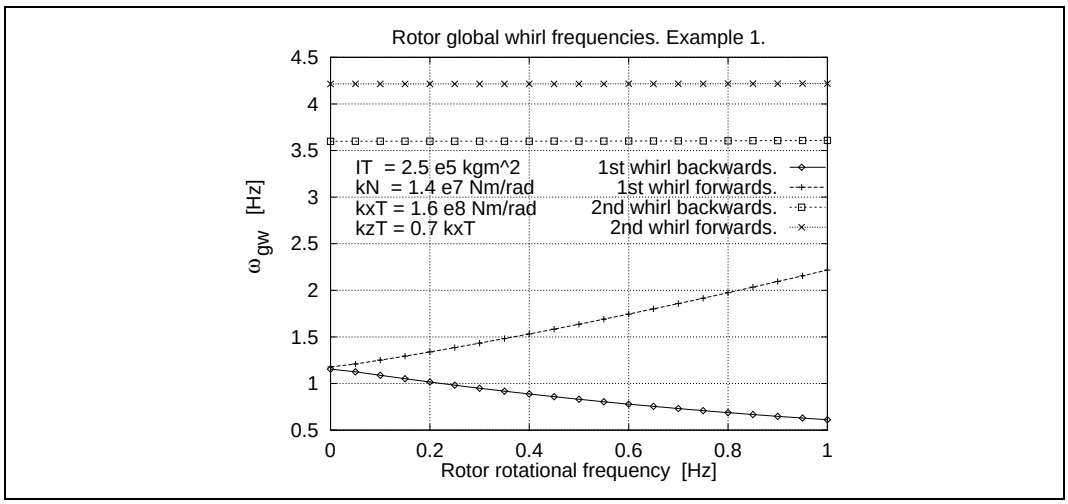

Figure 4.2. Natural frequencies for Example 1 as function of rotor speed.

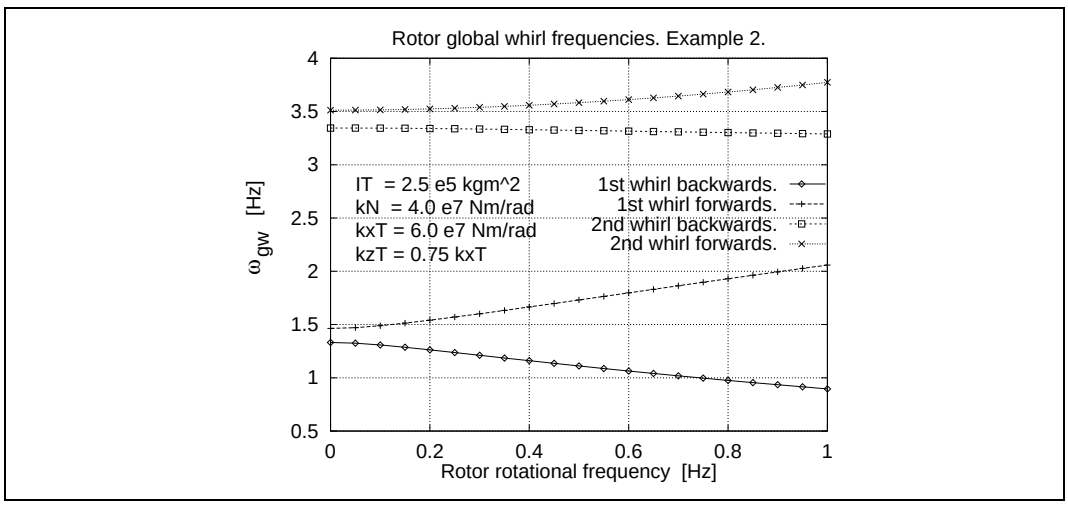

Figure 4.3. Natural frequencies for Example 2 as function of rotor speed.

5 Example decomposition of normal operation response

Below examples are presented using the theory from Section 3. The response from the example 500 kW turbine with 19.0 m blades is considered for two configurations of the turbine. We analyze 256 seconds of simulated response at 23 m/s for the basic turbine (case Si1) and for a configuration with increased shaft stiffness (case Si2), respectively. Time traces of the edgewise blade root bending moments for the two cases are presented in Figure 5.1. At the chosen wind speed the turbine operates in deep stall. In the basic case severe edgewise vibrations develop, while these vibrations are limited to a much lower level in the case with stiffer shaft.

As the analyses are based on the edgewise blade root moments, the proportionality factor K_{uM} from Equation 3.41 is involved in the calculations. The actual value of K_{uM} is approximately 1200 kNm/m.

Below the results for the two cases are presented in paired figures, where the left figure column covers the basic case, and the right figure column covers the configuration with increased shaft stiffness. Figure 5.2 shows 1 second of the time trace for all three blade tip deflections. Figure 5.3 shows the power spectral densities of the deflections. The edgewise vibration at 2.9 Hz dominates the response. The 1P frequency is approximately 0.5 Hz. In Figure 5.4 the time trace for blade 1 is shown for 2.5 rotor revolutions. The 1P component, calculated according to Equation 3.44, is shown in the figure. The discontinuities in the 1P curve are due to the averaging per rotor revolution and basically caused by the time varying 1P aero-load.

The plots in Figure 5.5 show the local blade whirl deformation components calculated according to Equations 3.33 and 3.34, respectively. They vary with time due to the time varying edgewise vibration. The whirl components are calculated for each complete cycle of the edgewise vibration, assuming that the vibration is harmonic during this period. A Fourier series expansion equivalent to the one for the 1P component in Equation 3.44 is applied, only, the period is now $T_P = \frac{2\pi}{\omega_e}$. It is observed that the backward (or retrograde) component is dominating. The corresponding, calculated in-plane inertia force is shown in the plots in Figure 5.6 for the time period 190-200 seconds. The arrows indicate that the rotation direction is backwards.

The tower top tilt and yaw bending moments for the same 190-200 seconds time period are shown in the plots in Figure 5.7, where the curves show the trace of the rotating moment at the tower top. The regular global rotor whirl pattern is clearly observed for the basic wind turbine configuration (left plot), whereas the whirl pattern for the configuration with increased shaft stiffness (right plot) is more chaotic, indicating that no dominating vibration mode is excited in this case. A 5 seconds period of the time traces of these moments are shown in Figure 5.8.

In Figure 5.9 the power spectral densities of the tower top moments are shown. The dominating rotating moment at the tower top shown in the left plot in Figure 5.7 has the frequency $\omega_e - \Omega \simeq 2.4$ Hz in accordance with the highest peak in the power spectrum. This frequency corresponds to the frequency of the dominating retrograde local blade whirl component, which acts as a forced excitation on the rotor whirl, and from investigations presented in Section 7 it turns out that this frequency is not a rotor whirl frequency. In the power spectrum the $\omega_e + \Omega \simeq 3.4$ Hz frequency is identified as well. This frequency is identical with the frequency of the progressive blade whirl component, and the investigations

in Section 7 show that it is very close to the 2^{nd} backward rotor whirl frequency as well. Both these frequencies seem to be essential for the coupling between *local blade whirl* and *global rotor whirl*, as confirmed by theory presented in the following Section 6, where the energy exchange between the whirl modes is investigated by use of an expression for work. This investigation shows that the actual values of the blade whirl frequencies relative to the rotor whirl frequencies decide the direction of the energy exchange, i.e. whether the forces associated with the blade whirl modes perform work on the rotor whirl modes or vice versa. In the present case a possible explanation is that energy is transferred from the progressive blade whirl mode, which ceases to vibrate, via the 2^{nd} backward rotor whirl mode to the retrograde blade whirl mode, which shows increased vibration level. The vibration levels of the blade whirl modes are most clearly seen in Figure 5.5.

As shown in the right plot in Figure 5.9 the response frequencies in the area around 3.4 Hz have changed for the configuration with stiffened shaft, obviously enough to prevent initiation of the global rotor whirl and the violent edgewise vibration. A possible interpretation based on the energy exchange theory is that the favourable conditions for energy exchange are no longer present due to the changed rotor whirl frequencies, and the energy is no longer concentrated on the retrograde blade whirl component.

The 2^{nd} rotor tilt and yaw frequencies at stand still are found from Table 2.1 to be 3.67 Hz and 4.36 Hz, respectively, for the original configuration, and 3.76 Hz and 4.97 Hz, respectively, for the stiffened configuration. These frequencies are changed during rotation as illustrated in Section 4 by the simple model. The subject is further pursued in Section 7, where a method for determining the rotor whirl frequencies by use of a general aeroelastic program is demonstrated. Here the relevant 2^{nd} backward rotor whirl frequency is found to approximately 3.4 Hz for case Si1 and 3.6 Hz for case Si2, respectively.

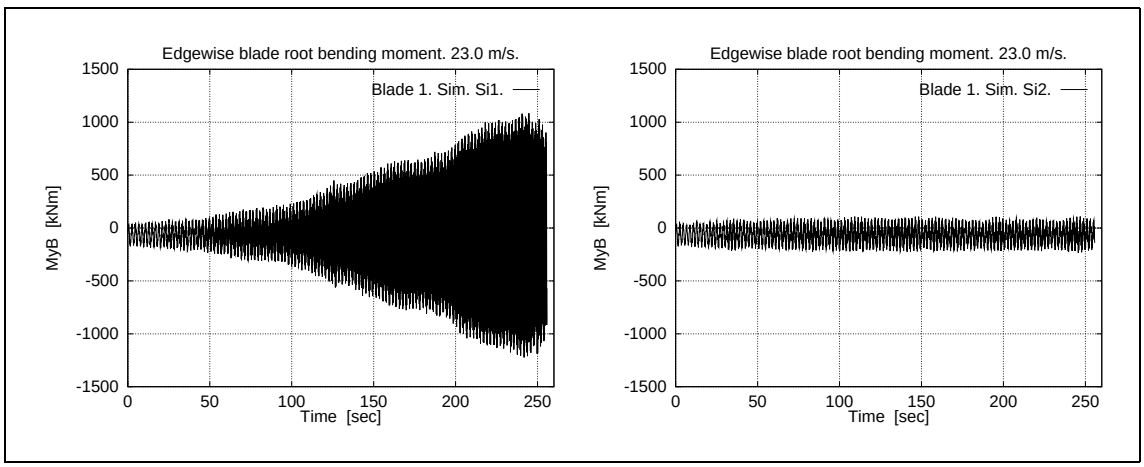

Figure 5.1. Simulated edgewise blade root moments. Left: *Basic case* Si1 *shows dominating, increasing vibration with the edgewise frequency.* Right: *Stiffened shaft case* Si2 *shows limited vibration.*

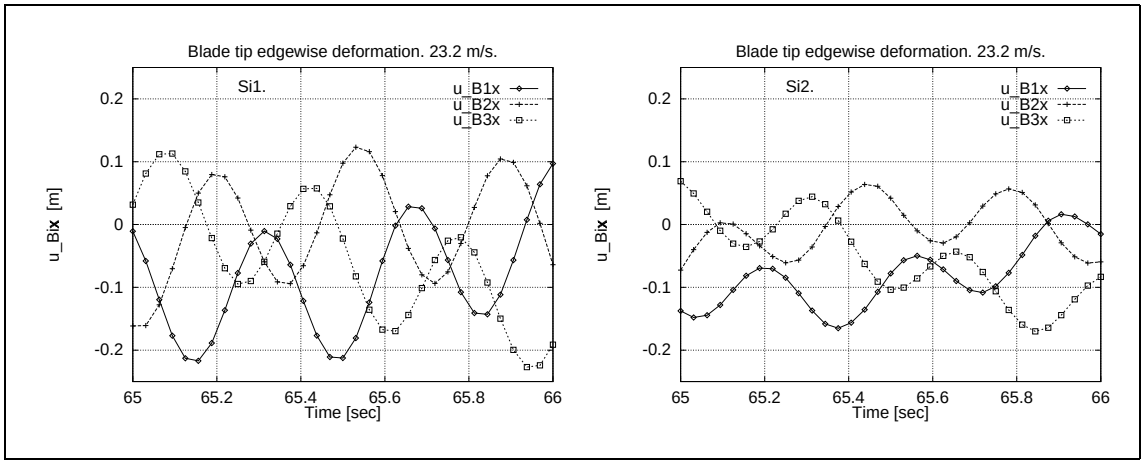

Figure 5.2. Time traces of edgewise deformations at the blade tip.

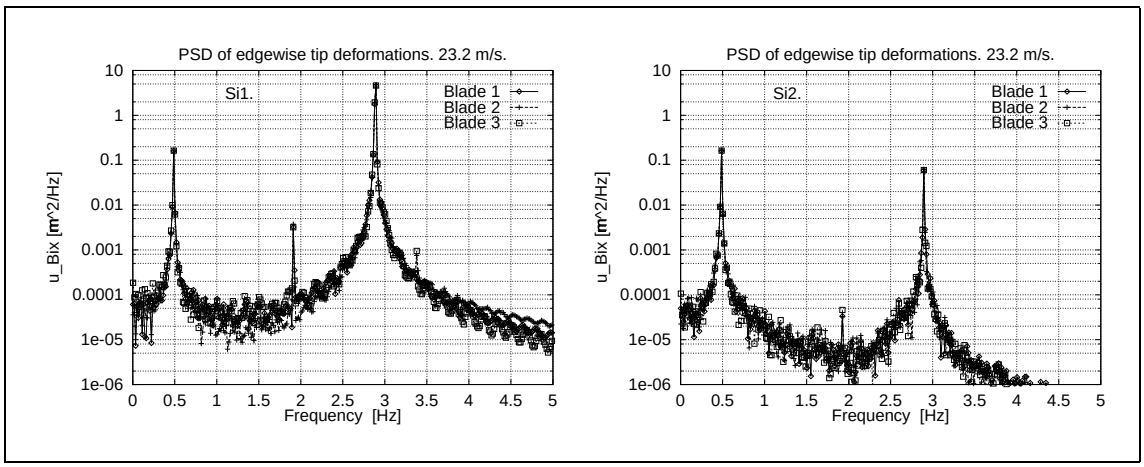

Figure 5.3. Power spectral densities of the total edgewise tip deflections.

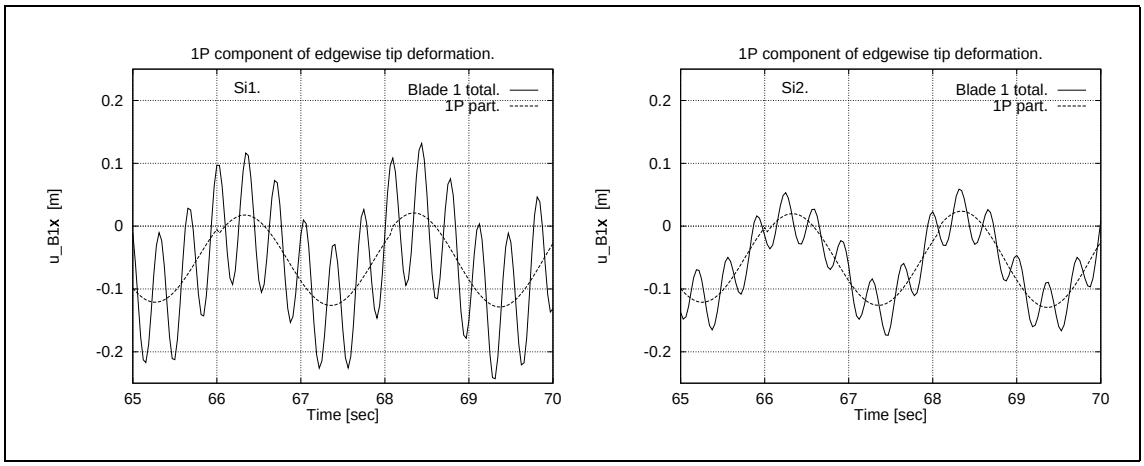

Figure 5.4. Total edgewise tip deflections and 1P component.

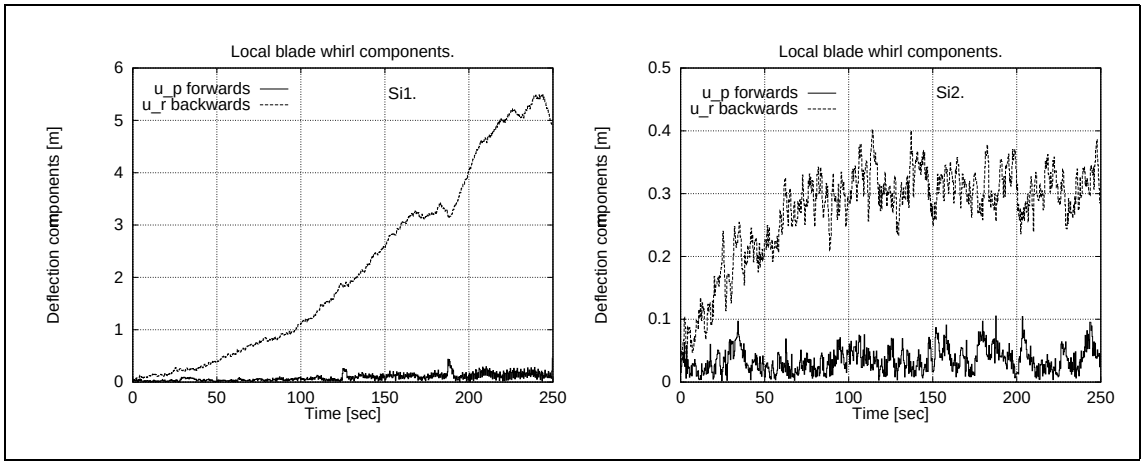

Figure 5.5. Local blade whirl deflection components.

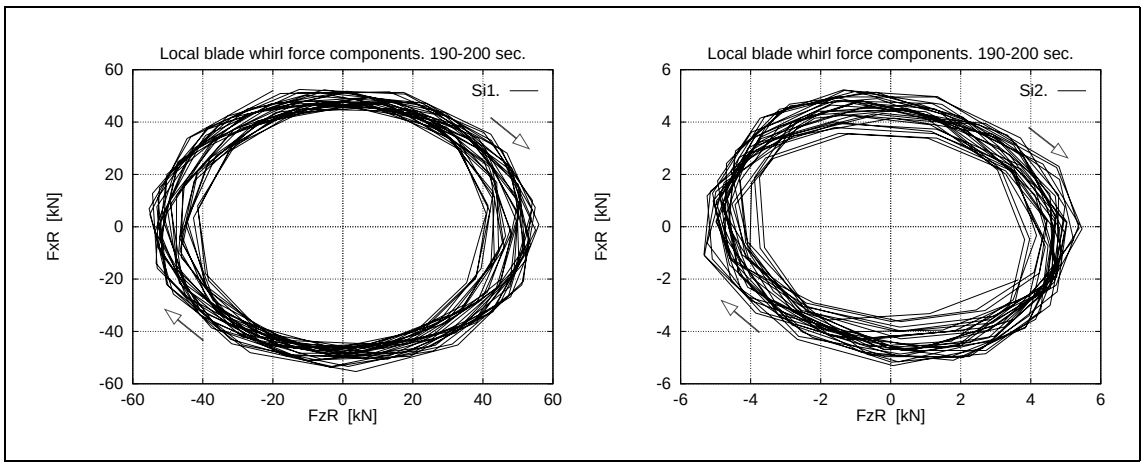

Figure 5.6. Components of local blade-whirl force. The arrows show the rotation direction.

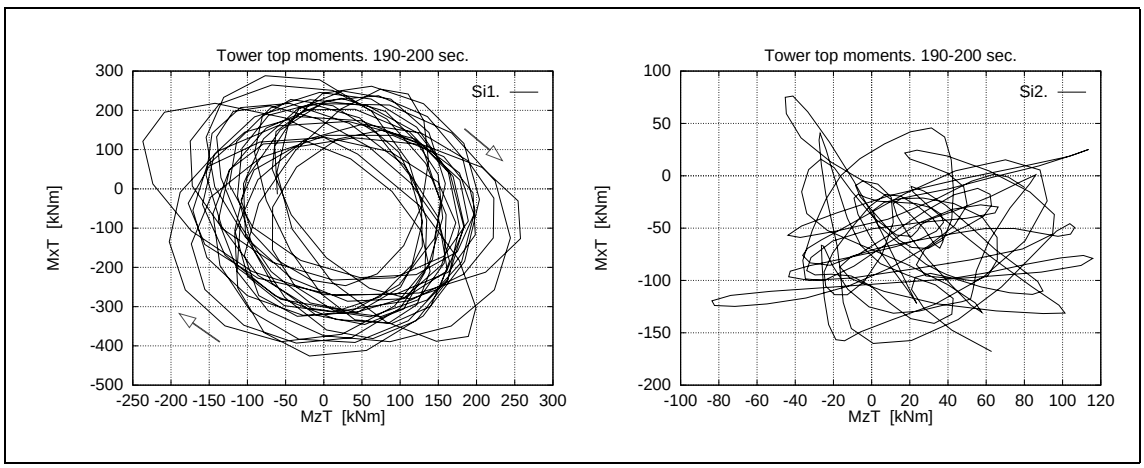

Figure 5.7. Tower top tilt and yaw bending moments. The arrows show the rotation direction.

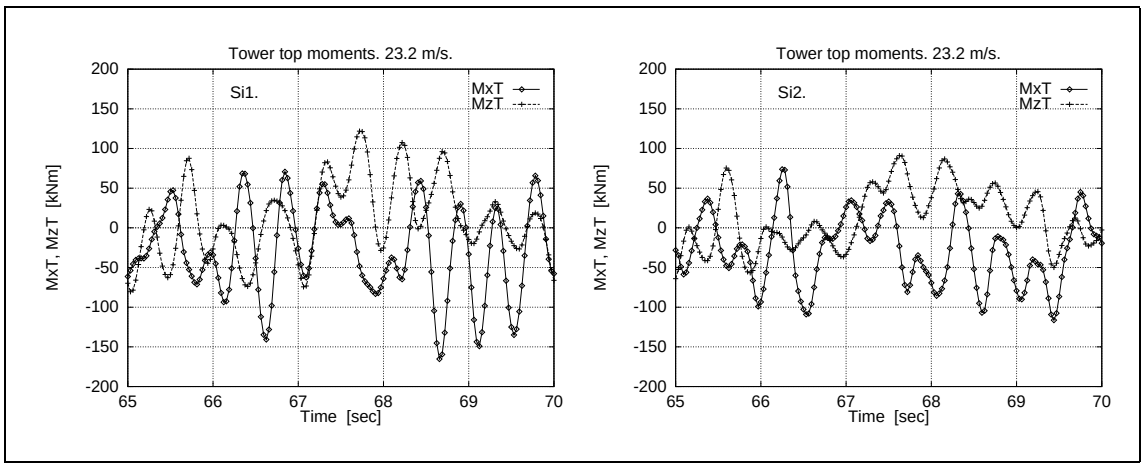

Figure 5.8. Time traces of tower top tilt and yaw moments.

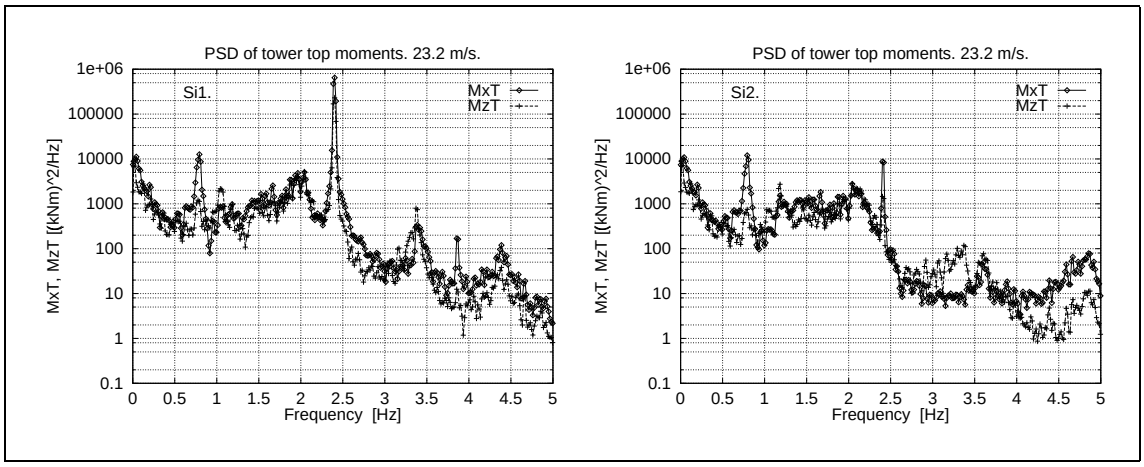

Figure 5.9. Power spectral densities of tower top moments.

6 Illustration of exchange of energy

The explanation for some of the observed response patterns in the previous sections might be found by looking at the energy exchange between local blade whirl and global rotor whirl. We do so in the present section by expressing the work performed by the in-plane inertia force – due to edgewise blade vibrations – on the global rotor whirl motion.

When a global whirl mode is excited, the movement of the hub in the vertical plane describes basically an elliptical path, as shown in Figure 4.1 in Section 4. This movement is described by the following vector with reference to stationary tower T-coordinates:

$$\left\{ \begin{array}{c} u_{xw}^T \\ u_{zw}^T \end{array} \right\} = \left[\begin{array}{cc} \sin(\omega_{gw}t + \gamma_{pw}) & -\sin(\omega_{gw}t + \gamma_{rw}) \\ \cos(\omega_{gw}t + \gamma_{pw}) & \cos(\omega_{gw}t + \gamma_{rw}) \end{array} \right] \left\{ \begin{array}{c} u_{pw} \\ u_{rw} \end{array} \right\}, \tag{6.1}$$

where the principles of resolving in the progressive and the retrograde components have been applied, as described previously for the force in Section 3.2. In this equation

u_{pw}	is the progressive displacement component,
u_{rw}	the retrograde displacement component,
γ_{pw}	the phase of the progressive component,
γ_{rw}	the phase of the retrograde component and
ω_{gw}	is the global rotor whirl frequency.

The velocity vector of the rotor center movement is obtained by differentiation of the displacement with respect to time:

$$\left\{ \begin{array}{c} \dot{u}_{xw}^T \\ \dot{u}_{zw}^T \end{array} \right\} = \omega_{gw} \left[\begin{array}{cc} \cos(\omega_{gw}t + \gamma_{pw}) & -\cos(\omega_{gw}t + \gamma_{rw}) \\ -\sin(\omega_{gw}t + \gamma_{pw}) & -\sin(\omega_{gw}t + \gamma_{rw}) \end{array} \right] \left\{ \begin{array}{c} u_{pw} \\ u_{rw} \end{array} \right\}. \tag{6.2}$$

The in-plane inertia force vector associated with the edgewise vibration is repeated from Equation 3.28. In stationary T-coordinates it was found to:

$$\left\{ \begin{array}{c} F_x^T \\ F_z^T \end{array} \right\} = \left[\begin{array}{cc} \sin\left[(\omega_e + \Omega)\,t + \gamma_{Fp}\right] & -\sin\left[(\omega_e - \Omega)\,t + \gamma_{Fr}\right] \\ \cos\left[(\omega_e + \Omega)\,t + \gamma_{Fp}\right] & \cos\left[(\omega_e - \Omega)\,t + \gamma_{Fr}\right] \end{array} \right] \left\{ \begin{array}{c} F_p \\ F_r \end{array} \right\}. \tag{3.28}$$

The meaning of the symbols is revived:

F_p	is the progressive force component,
F_r	the retrograde force component,
γ_{Fp}	the phase of the progressive component,
γ_{Fr}	the phase of the retrograde component,
ω_e	the edgewise blade frequency and
Ω	is the rotor rotation frequency.

The work per unit time (the power) performed by the in-plane inertia force on the hub – and through that on the global rotor whirl – is obtained by the scalar product of the force and the hub transverse velocity according to:

$$
\begin{aligned}
\dot{W} &= \left\{ \begin{array}{c} F_x^T \\ F_z^T \end{array} \right\}^T \left\{ \begin{array}{c} \dot{u}_{xw}^T \\ \dot{u}_{zw}^T \end{array} \right\} \\
&= -\omega_{gw}\Big(F_p \cos[(\omega_e+\Omega)t+\gamma_{Fp}] + F_r \cos[(\omega_e-\Omega)t+\gamma_{Fr}]\Big) \\
&\qquad \Big(u_{pw}\sin[\omega_{gw}t+\gamma_{pw}] + u_{rw}\sin[\omega_{gw}t+\gamma_{rw}]\Big) \\
&\quad + \omega_{gw}\Big(F_p \sin[(\omega_e+\Omega)t+\gamma_{Fp}] - F_r \sin[(\omega_e-\Omega)t+\gamma_{Fr}]\Big) \\
&\qquad \Big(u_{pw}\cos[\omega_{gw}t+\gamma_{pw}] - u_{rw}\cos[\omega_{gw}t+\gamma_{rw}]\Big) \,. \qquad (6.3)
\end{aligned}
$$

Finally, this power expression is integrated over a time period corresponding to n cycles of the global rotor whirl motion:

$$
t = \frac{n2\pi}{w_{gw}} \,, \qquad (6.4)
$$

and a function for the work performed by the in-plane inertia force on the global whirl motion is obtained. The integration gives the function

$$
\begin{aligned}
&W\left(F_p, F_r, \gamma_{Fp}, \gamma_{Fr}, u_{pw}, u_{rw}, \gamma_{pw}, \gamma_{rw}, \omega_{gw}, \omega_e, \Omega, n\right) = \int_{t=0}^{\frac{n2\pi}{\omega_{gw}}} \dot{W}\,\mathrm{d}t \\
&= \frac{\omega_{gw}}{(\Omega-\omega_{gw}-\omega_e)(\Omega+\omega_{gw}-\omega_e)(\Omega-\omega_{gw}+\omega_e)(\Omega+\omega_{gw}+\omega_e)} \times \\
&\quad \Bigg[F_p u_{pw}\Big(\Omega^3+\Omega^2\omega_{gw}-\Omega\omega_{gw}^2-\omega_{gw}^3-\Omega^2\omega_e-2\Omega\omega_{gw}\omega_e-\omega_{gw}^2\omega_e-\Omega\omega_e^2 \\
&\qquad + \omega_{gw}\omega_e^2+\omega_e^3\Big)\left(\cos\left[\gamma_{pw}-\gamma_{Fp}\right]-\cos\left[\gamma_{pw}-\gamma_{Fp}-n2\pi\frac{\omega_e+\Omega}{\omega_{gw}}\right]\right) \\
&\quad + F_p u_{rw}\Big(-\Omega^3+\Omega^2\omega_{gw}+\Omega\omega_{gw}^2-\omega_{gw}^3+\Omega^2\omega_e-2\Omega\omega_{gw}\omega_e+\omega_{gw}^2\omega_e+\Omega\omega_e^2 \\
&\qquad + \omega_{gw}\omega_e^2-\omega_e^3\Big)\left(\cos\left[\gamma_{rw}+\gamma_{Fp}\right]-\cos\left[\gamma_{rw}+\gamma_{Fp}+n2\pi\frac{\omega_e+\Omega}{\omega_{gw}}\right]\right) \\
&\quad + F_r u_{rw}\Big(-\Omega^3+\Omega^2\omega_{gw}+\Omega\omega_{gw}^2-\omega_{gw}^3-\Omega^2\omega_e+2\Omega\omega_{gw}\omega_e-\omega_{gw}^2\omega_e+\Omega\omega_e^2 \\
&\qquad + \omega_{gw}\omega_e^2+\omega_e^3\Big)\left(\cos\left[\gamma_{rw}-\gamma_{Fr}\right]-\cos\left[\gamma_{rw}-\gamma_{Fr}-n2\pi\frac{\omega_e-\Omega}{\omega_{gw}}\right]\right) \\
&\quad + F_r u_{pw}\Big(\Omega^3+\Omega^2\omega_{gw}-\Omega\omega_{gw}^2-\omega_{gw}^3+\Omega^2\omega_e+2\Omega\omega_{gw}\omega_e+\omega_{gw}^2\omega_e-\Omega\omega_e^2 \\
&\qquad + \omega_{gw}\omega_e^2-\omega_e^3\Big)\left(\cos\left[\gamma_{pw}+\gamma_{Fr}\right]-\cos\left[\gamma_{pw}+\gamma_{Fr}+n2\pi\frac{\omega_e-\Omega}{\omega_{gw}}\right]\right)\Bigg]. \qquad (6.5)
\end{aligned}
$$

Apparently, the work function has two singularities in the frequency range of interest. One for $\omega_{gw} = \Omega - \omega_e$ and another for $\omega_{gw} = \Omega + \omega_e$. However, they both turn out to be removable.

The energy exchange is investigated for a range of cases with different assumptions. These examples are chosen to illustrate the full scale simulations in Section 5, and especially the influence of the presence of either one or both of the in-plane force components, F_p and F_r, and of either one or both of the rotor whirl components, u_{pw} and u_{rw}. The parameters for the selected cases are listed in Table 6.1.

Table 6.1. Parameters for work expression examples.

Parameter	Units	Figures									
		6.2		6.3		6.4		6.5		6.6	
F_p	[kN]	10.00	0.00	10.00	0.00	10.00	0.00	10.00	0.00	10.00	0.00
F_r	[kN]	0.00	10.00	0.00	10.00	0.00	10.00	0.00	10.00	0.00	10.00
γ_{Fp}	[°]	0.00		0.00		0.00		0.00		0.00	
γ_{Fr}	[°]	0.00		0.00		0.00		0.00		0.00	
u_{pw}	[m]	0.15		0.15		0.15		0.15		0.00	
u_{rw}	[m]	0.25		0.25		0.25		0.00		0.25	
γ_{pw}	[°]	0.00		0.00		0.00		0.00		0.00	
γ_{rw}	[°]	0.00		0.00		0.00		0.00		0.00	
ω_{gw}	[Hz]	Variable		Variable		Variable		Variable		Variable	
ω_e	[Hz]	2.90		2.90		2.90		2.90		2.90	
Ω	[Hz]	0.50		0.50		0.50		0.50		0.50	
n	[cycles]	1		5		20		5		5	

In all the examples the phase angles are assumed to be zero. The blade edgewise frequency is constant, $\omega_e = 2.9$ Hz, and so is the rotor rotational speed, $\Omega = 0.5$ Hz. The global rotor whirl frequency, ω_{gw}, is varied, and the influence of the number of rotor whirl integration cycles is illustrated. In the figures below the results are plotted in pairs, such that one curve shows the result with only the progressive in-plane force, F_p, present, and the other curve shows the results with only the retrograde component, F_r, present. For such one pair of results all other parameters are kept identical.

For the three first double examples – with reference to Figures 6.2-6.4 – both the progressive and the retrograde components of the rotor whirl motion are present (u_{pw} and u_{rw}), and the movement of the rotor center during the whirl motion follows an elliptical path in the retrograde direction as shown in Figure 6.1. This is similar to the movement pattern, which would be expected for the 2^{nd} rotor whirl mode at approximately 3.4 Hz for the basic example in Section 5.

The energy exchange for the chosen cases are calculated by use of the work function in Equation 6.5. The results are shown in Figures 6.2-6.6 as function of global rotor whirl frequency. When the work is positive it means that the in-plane inertia force performs work on the global rotor whirl, and when it is negative, the energy is transferred from the rotor whirl to the edgewise vibration.

The results of the three first double cases – presented in Figures 6.2-6.4 – show that the progressive in-plane force component performs work on the rotor whirl below $\omega_{gw} = \omega_e + \Omega = 3.4$ Hz, and that the rotor whirl performs work on the edgewise vibration above this frequency. The same is valid for the retrograde in-plane component, only the sign changes at $\omega_{gw} = \omega_e - \Omega = 2.4$ Hz. Between these two frequencies the two in-plane local blade whirl components can exchange energy via the global rotor whirl mode, such that the energy is transferred from the progressive to the retrograde component of the local blade whirl, and the vibration corresponding to the retrograde component is amplified.

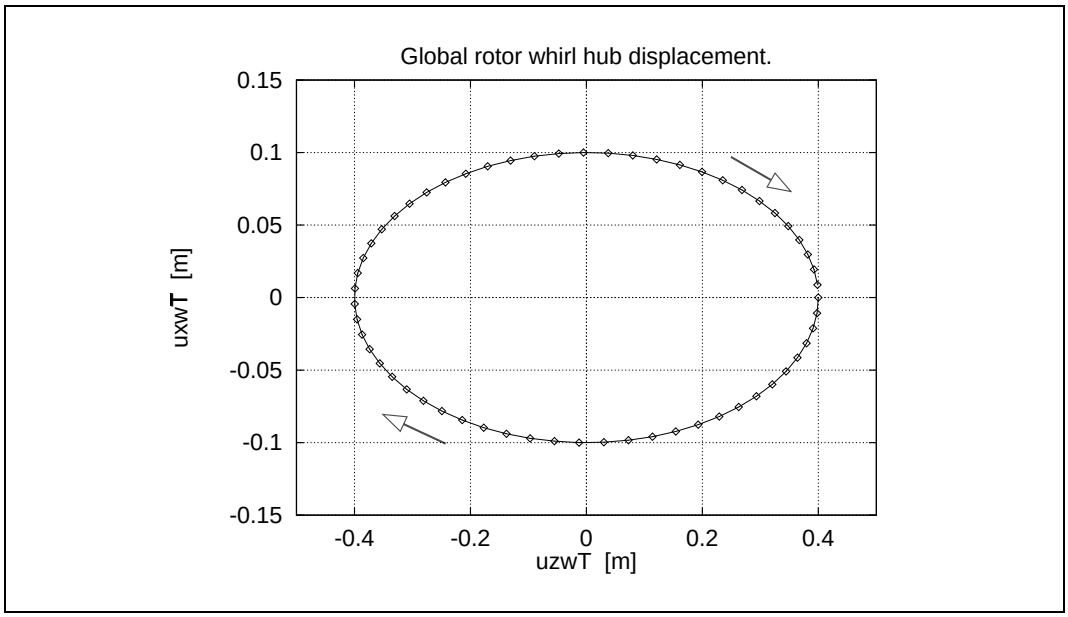

Figure 6.1. Movement of the rotor center corresponding to global rotor whirl in the examples. The arrows show the direction of rotation.

Assuming that the involved global whirl frequency in the basic case in Section 5 is just below $\omega_{gw} = \omega_e + \Omega = 3.4$ Hz, this is a probable explanation for the results shown in the left plot in Figure 5.5, where the retrograde blade vibration component increases. The right plot in the figure, corresponding to the configuration with stiffened shaft, shows much less pronounced increase of the retrograde component, probably due to the changed energy exchange at the corresponding higher frequency above $\omega_{gw} = \omega_e + \Omega = 3.4$ Hz. In Section 7 it is shown that the frequency is increased to approximately 3.6 Hz.

It is observed that the major influence of increasing the number of integration cycles, n, is that the work peaks are moved towards the frequencies, where the work function changes sign, $\omega_{gw} = 2.4$ Hz and $\omega_{gw} = 3.4$ Hz. The levels of the peaks are almost unchanged.

The results of the last two parameter settings from Table 6.1 presented in Figures 6.5 and 6.6 show that the progressive in-plane inertia force component can only perform work on or interact with the progressive rotor whirl component and vice versa.

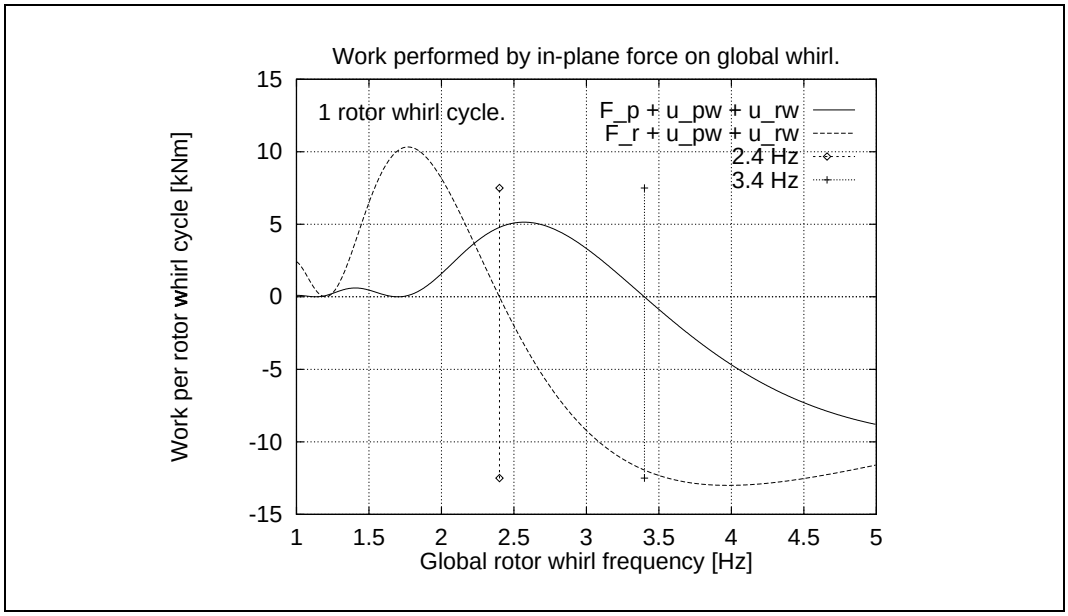

Figure 6.2. Energy exchange between blade edgewise vibration and rotor whirl as function of rotor whirl frequency, ω_{gw}. The energy is the average of 1 complete rotor whirl cycle.

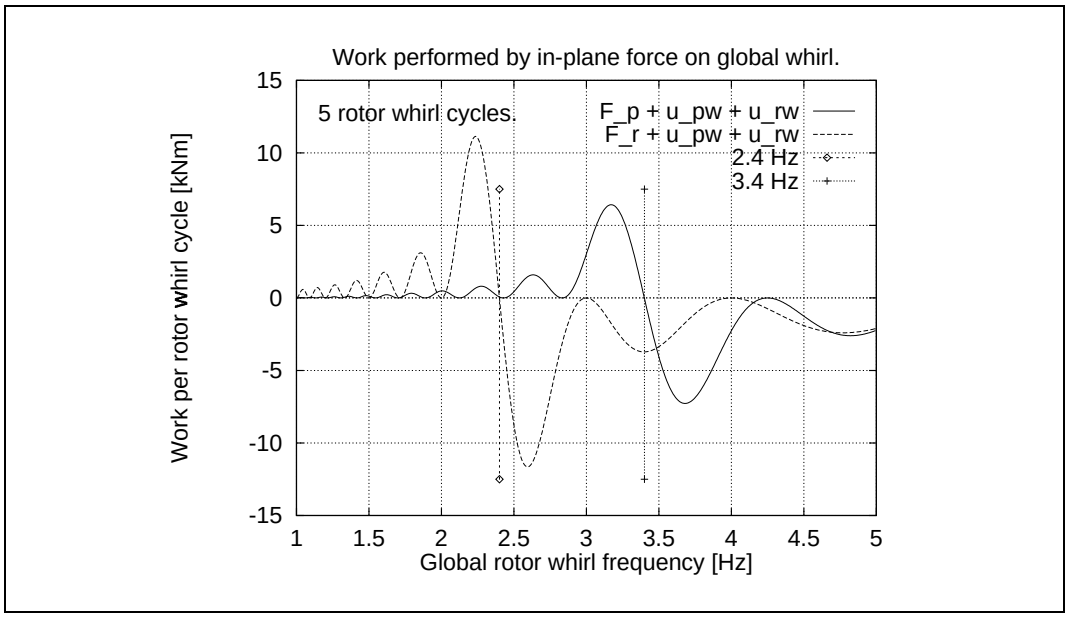

Figure 6.3. Energy exchange between blade edgewise vibration and rotor whirl as function of rotor whirl frequency, ω_{gw}. The energy is the average of 5 complete rotor whirl cycles.

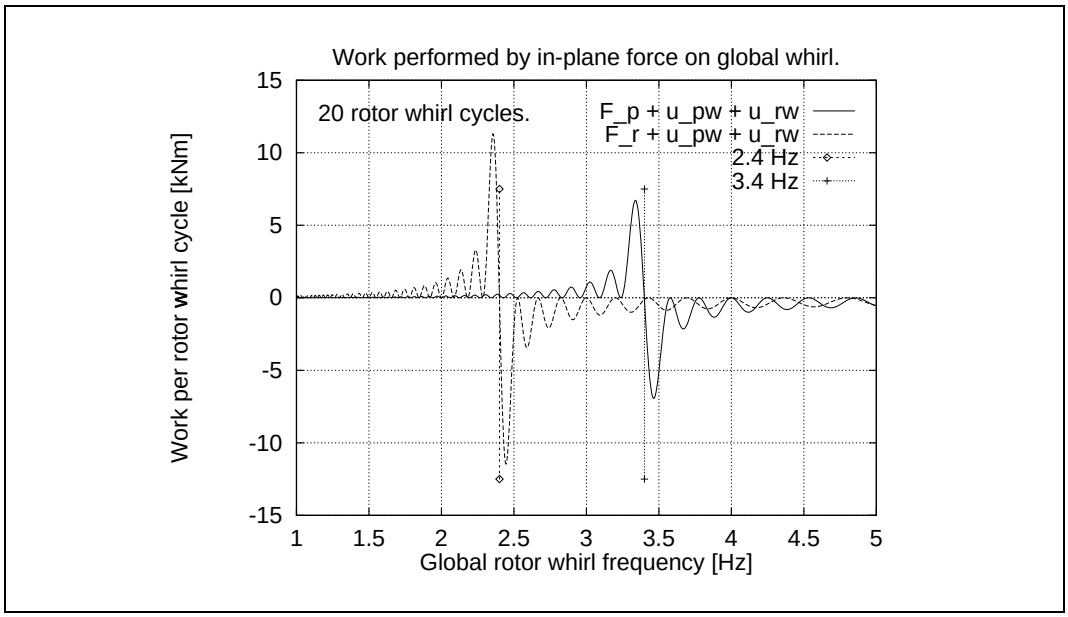

Figure 6.4. Energy exchange between blade edgewise vibration and rotor whirl as function of rotor whirl frequency, ω_{gw}. The energy is the average of 20 complete rotor whirl cycles.

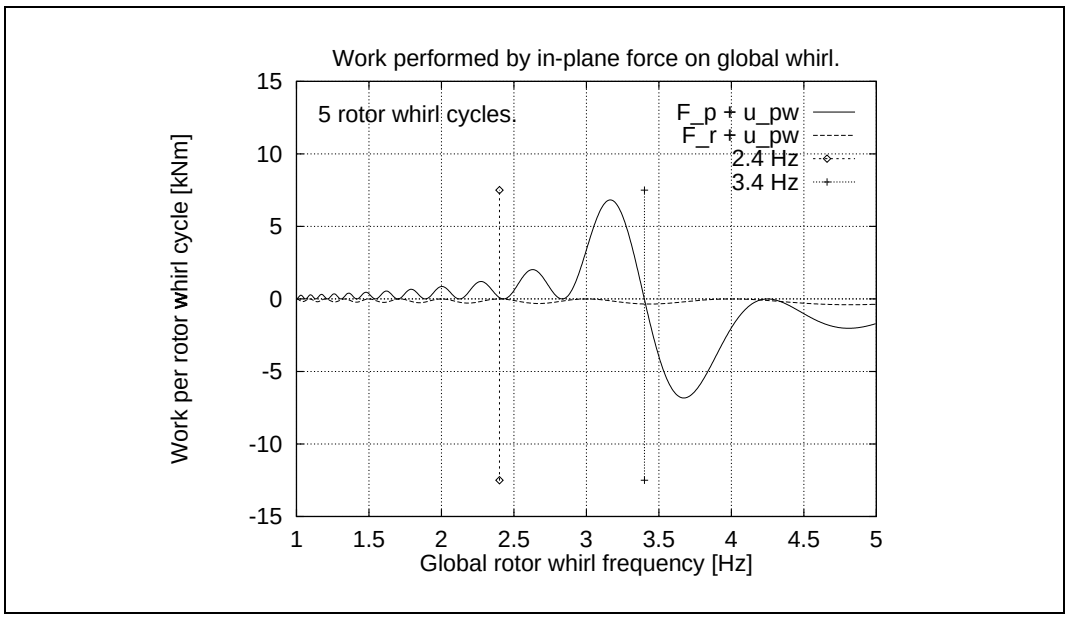

Figure 6.5. Energy exchange between blade edgewise vibration and rotor whirl as function of rotor whirl frequency, ω_{gw}. Only the progressive global rotor whirl component, u_{pw}, is present. The energy is the average of 5 complete rotor whirl cycles.

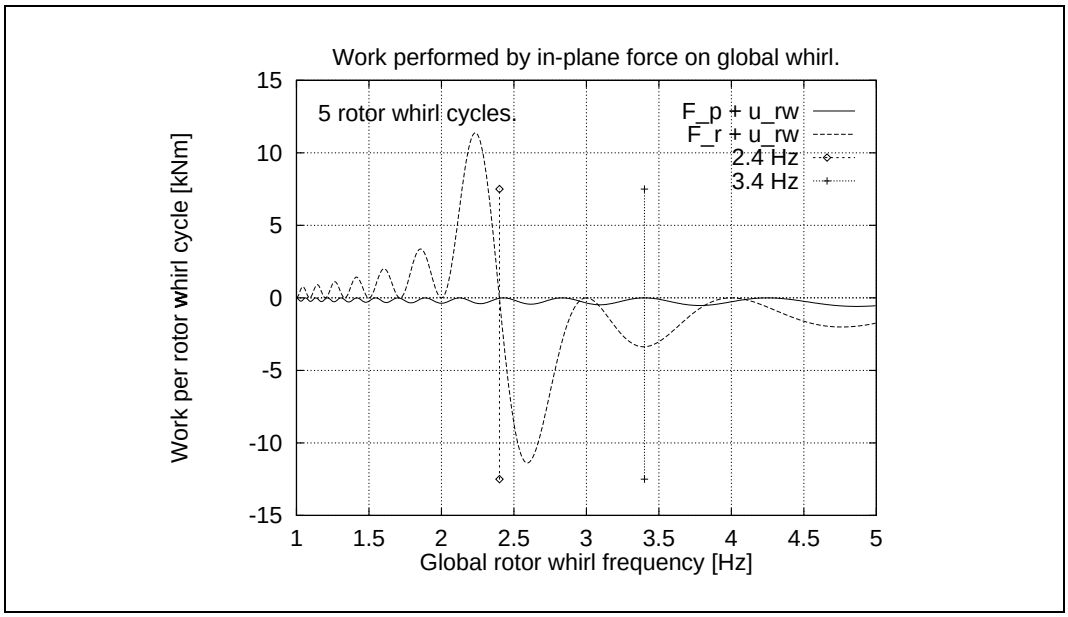

Figure 6.6. Energy exchange between blade edgewise vibration and rotor whirl as function of rotor whirl frequency, ω_{gw}. Only the retrograde global rotor whirl component, u_{rw}, is present. The energy is the average of 5 complete rotor whirl cycles.

7 Identification of global whirl modes by excitation

The influence of the wind turbine global structural dynamics on the edgewise blade vibration phenomena is illustrated for instance in Section 5 in Figure 5.1. In this figure the simulated edgewise blade root moments of two different wind turbine configurations are shown. The turbine is operating in stall at 23 m/s. It is seen that one of the configurations is subject to severe edgewise vibrations. The difference between the two cases is different shaft stiffnesses.

As pointed out previously, the actual values of the local blade whirl frequencies and the global rotor whirl frequencies are important for the interaction between the two vibrations – if the frequencies are close to each other, a significant energy exchange might take place, and both vibrations might develop more easily than otherwise. Further, the investigation of energy exchange in the previous section indicates that the edgewise blade vibration is more likely developed, if the rotor whirl frequency lies between the blade whirl frequencies as seen in the stationary frame of reference. In a design situation it might therefore be of interest to gain some knowledge about their actual values in order to try to avoid the coupling by proper design choices.

Normally, the blade frequency is easy to determine, as it usually can be detected very clearly from the power spectral densities of normal operation response. Further, it will be rather close to the non-rotating blade frequency, which can be determined from an eigenvalue analysis. The opposite is the case for the rotor whirl frequencies. They are difficult to detect directly from the power spectra of normal operation response. Primarily, because they are less pronounced in the spectra and often in the vicinity of other frequencies. An eigenvalue analysis of the non-rotating turbine is not directly applicable, as the rotating frequencies might deviate significantly from the stand-still frequencies due to gyroscopic forces as shown in Section 4.

Below we demonstrate a method for finding the approximate values of the rotor whirl frequencies. The method is based on excitation during operation with a known harmonic moment at the tower top.

Determination of global rotor whirl frequencies

The global rotor whirl frequencies can be approximately determined by use of an aeroelastic code. During operation the whirl modes can be excited by use of harmonic forces or moments, and analysis of the response, e.g. by calculation of the power spectral densities, can provide the frequency values. We demonstrate a method, where the whirl modes are excited by a harmonic moment at the tower top. The frequency of the moment, $f_e(t)$, is varied linearly during the calculation period, T. The variation of the excitation frequency around a chosen center frequency, f_c, follows the expression

$$f_e(t) = f_c \left(1 - p + 2p\frac{t}{T}\right) , \tag{7.1}$$

where p is the percentage the variable frequency lies below the center frequency at time $t = 0$ sec and above at $t = T$ sec.

The applied excitation is equivalent to the inherent excitation by the harmonic force from the local blade whirl described in Section 3, but it is obtained by applying a time varying moment at the tower top as shown in Figure 2.4, where the moment components, M_x and M_z,

vary harmonically with the amplitude M_0 and with the specified frequency, f_e, according to

$$\left\{ \begin{array}{c} M_x(t) \\ M_y(t) \\ M_z(t) \end{array} \right\} = \left\{ \begin{array}{c} M_0 \cos\left(2\pi f_c \left[(1-p)\,t + p\frac{t^2}{T}\right]\right) \\ 0 \\ \pm M_0 \sin\left(2\pi f_c \left[(1-p)\,t + p\frac{t^2}{T}\right]\right) \end{array} \right\}, \tag{7.2}$$

which results in a constant size moment rotating in the vertical plane with the time dependent frequency $f_e(t)$. The moment with negative sin-term in the M_z component rotates in the same direction as the rotor, and we denote this direction the *forward* direction. The moment with positive sin-term in the M_z component rotates in the opposite direction of the rotor, and this direction is denoted the *backward* direction. Due to the varying frequency we refer to the excitations as either forward or backward *sweep*.

The results of aeroelastic calculations with excitation moments rotating *forwards* and *backwards*, respectively, are shown in the figures below for both the original basic turbine configuration, Si1, and the configuration with stiffened shaft, Si2. In the calculations M_0 is 2.5 kNm, f_c is 3.0 Hz and p is 60%. The gravity and the aerodynamic force are eliminated in the calculations. The structural damping is increased with a factor 2, resulting in a structural damping of approximately 5% logarithmic decrement. The plots in the figures with the results are arranged in pairs, and in general the results from the forward sweep excitation are in the left plot and the results from the backward sweep excitation are in the right plot.

Figure 7.1 shows the time traces of the tower top tilt moment, M_x^T, for the original configuration. The moment is recorded in the stationary tower coordinates. From the plots the approximate values of the rotor whirl frequencies can be detected in the ranges, where resonance is observed. At time $t = 0$ sec the resonance corresponds to the 1^{st} backward whirl frequency, at time $t = 140$ sec to the 1^{st} forward whirl frequency, at $t = 380$ sec to the 2^{nd} backward frequency and finally at $t = 520$ sec to the 2^{nd} forward frequency. Two peaks are observed in the range where the 2^{nd} backward mode is excited. This indicates that different coupling patterns exist, probably due to different participation of the blade flapwise modes.

The frequencies can also be detected from the power spectral densities of the tower top moments as presented in the plots in Figure 7.3. The approximate values of the whirl frequencies are:

- 1^{st} backward frequency $\simeq$ 1.1 Hz,
- 1^{st} forward frequency $\simeq$ 2.1 Hz,
- 2^{nd} backward frequency $\simeq$ 3.4 Hz and
- 2^{nd} forward frequency $\simeq$ 4.3 Hz.

Figures 7.2 and 7.4 show the corresponding time traces and power spectral densities for the turbine configuration with stiffened shaft. It is observed that all the whirl frequencies are increased with approximately 0.1-0.2 Hz. Especially the change of the 2^{nd} backward whirl frequency from 3.4 Hz to 3.6 Hz seems to be important for the coupling to the blade vibrations. The 3.4 Hz is the blade whirl frequency +1P. The change of the whirl frequency by +0.2 Hz is obviously important enough to reduce the influence from coupling. As shown in Section 6 probably due to the fact that the progressive and the retrograde blade whirl components no longer can exchange energy via the rotor whirl mode, when the rotor whirl frequency is outside the interval delimited by the blade whirl frequencies referred to stationary coordinates.

The time traces of the tower top response moments for the original configuration are shown as xy-plots in Figures 7.5 and 7.6 for the case with backward sweep excitation. Figure 7.5 shows the moments corresponding to 1^{st} backward and 1^{st} forward rotor whirl modes, respectively. Figure 7.6 shows the 2^{nd} backward and 2^{nd} forward whirl moments, respectively. The arrows in the plots show the rotation direction. The plots cover 16 sec of the time traces in the areas where the resonance peaks are detected from the right plot in Figure 7.1.

The plot of the 1^{st} backward whirl mode covers 16 sec from t =0 sec, the 1^{st} forward whirl 16 sec from t =140 sec, the 2^{nd} backward whirl 16 sec from t =380 sec and finally the 2^{nd} forward whirl 16 sec from t = 520 sec. The arrows in the plots indicate the rotation direction. By appropriate scaling of the shown moments the corresponding movement of the rotor center would be obtained with good approximation. So, the plots can also be viewed as the movement of the rotor center in a vertical plane.

For completeness, the power spectra of the blade root bending moments and the shaft bending moment are shown in the Figures 7.7-7.13 together with spectra of different combinations of tower top moments. The shaft bending moment, M_x^S, is recorded on the rotating shaft. The tower top moments, tilt M_x^T and yaw M_z^T, are recorded in the stationary tower coordinates.

The results show that the response is almost identical, whether the excitation is forward or backward, yet with the tendency that the whirl modes with the same rotation direction as the external moment are excited more easily than the modes with opposite whirl direction.

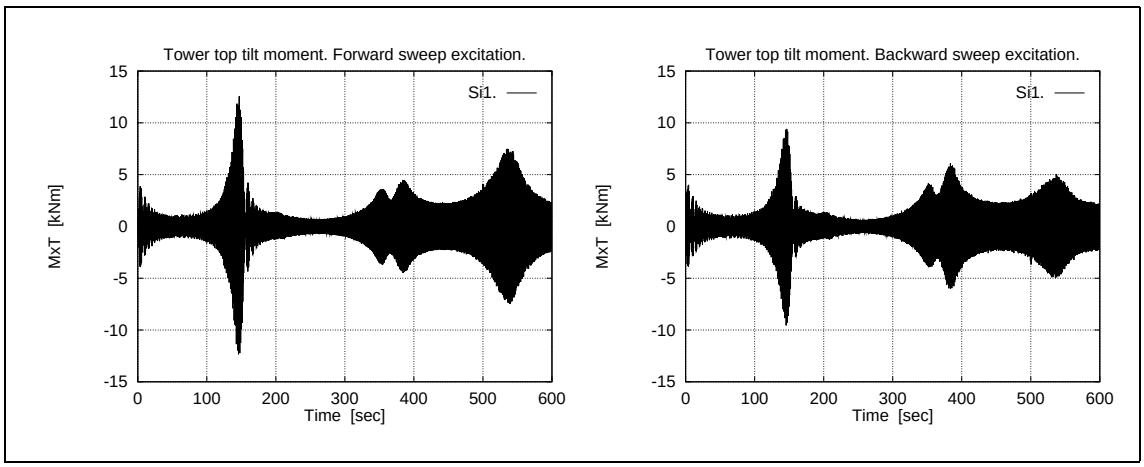

Figure 7.1. Case with original shaft stiffness. Tower top tilt moment, M_x^T, during excitation with harmonic moment with linearly varying frequency at the tower top. Left: *The excitation moment rotates forwards.* Right: *The excitation moment rotates backwards.*

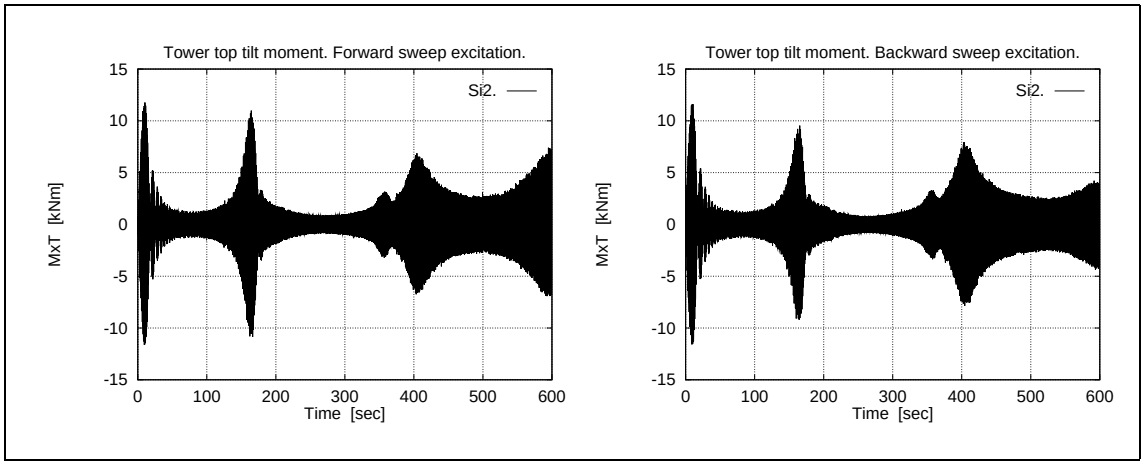

Figure 7.2. Case with stiffened shaft.Tower top tilt moment, M_x^T, during excitation with harmonic moment with linearly varying frequency at the tower top. Left: *The excitation moment rotates forwards.* Right: *The excitation moment rotates backwards.*

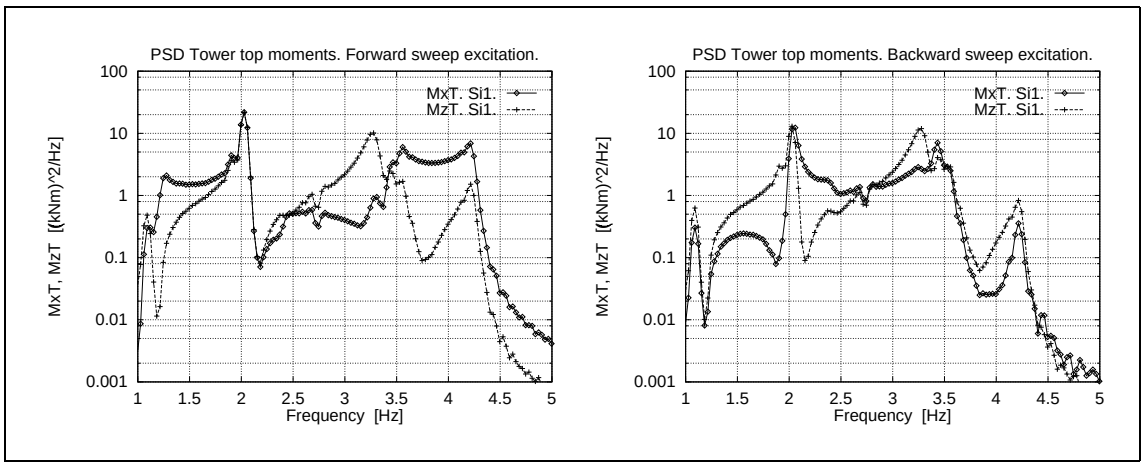

Figure 7.3. Power spectral density of tower top moments for the whole 10 minutes sweep period. Tilt moment, M_x^T, and yaw moment, M_z^T. Original stiffness. Left: *Forward excitation.* Right: *Backward excitation.*

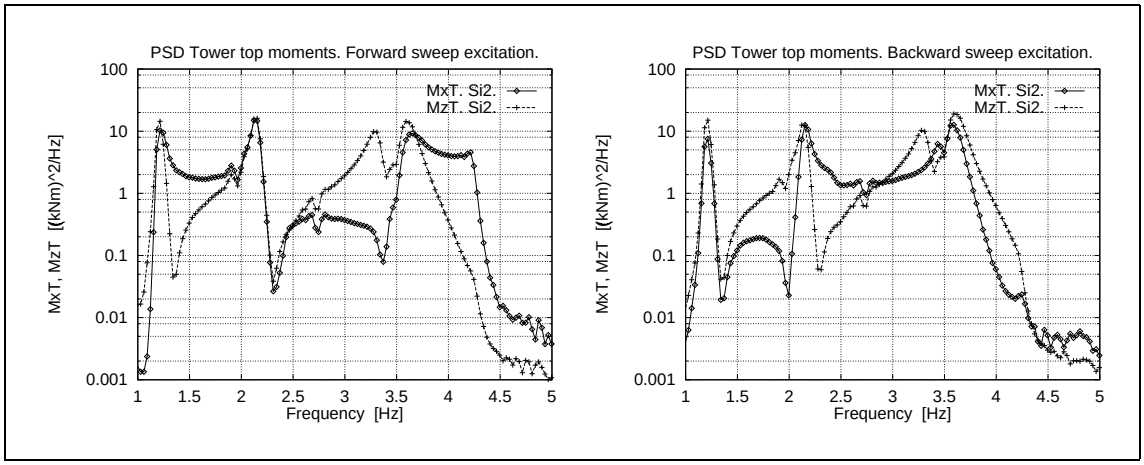

Figure 7.4. Power spectral density of tower top moments for the whole 10 minutes sweep period. Tilt moment, M_x^T, and yaw moment, M_z^T. Stiffened shaft. Left: *Forward excitation.* Right: *Backward excitation.*

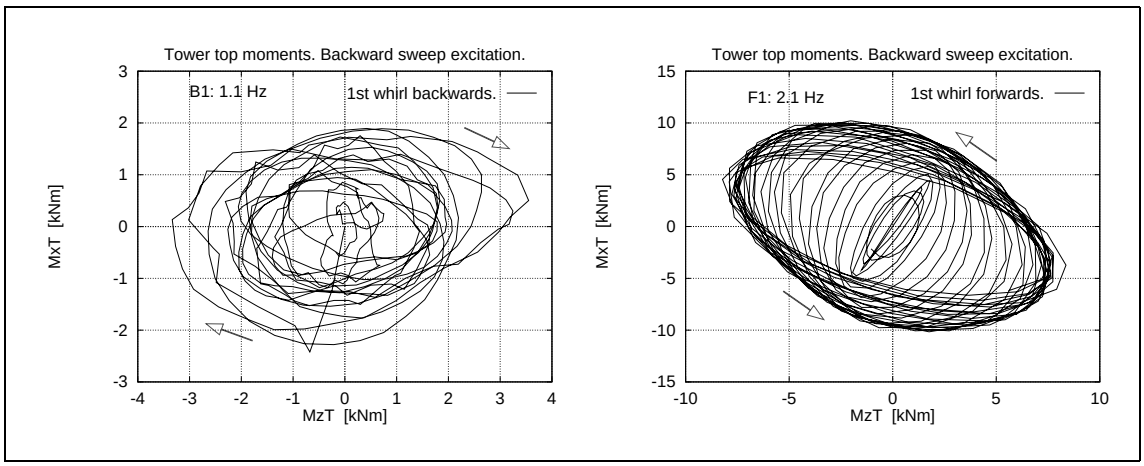

Figure 7.5. Tower top moments during excitation with harmonic moment with linearly varying frequency at the tower top. Tilt moment, M_x^T, and yaw moment, M_z^T. Left: *1^{st} whirl mode, whirling backwards, 1.1 Hz.* Right: *1^{st} whirl mode, whirling forwards, 2.1 Hz.*

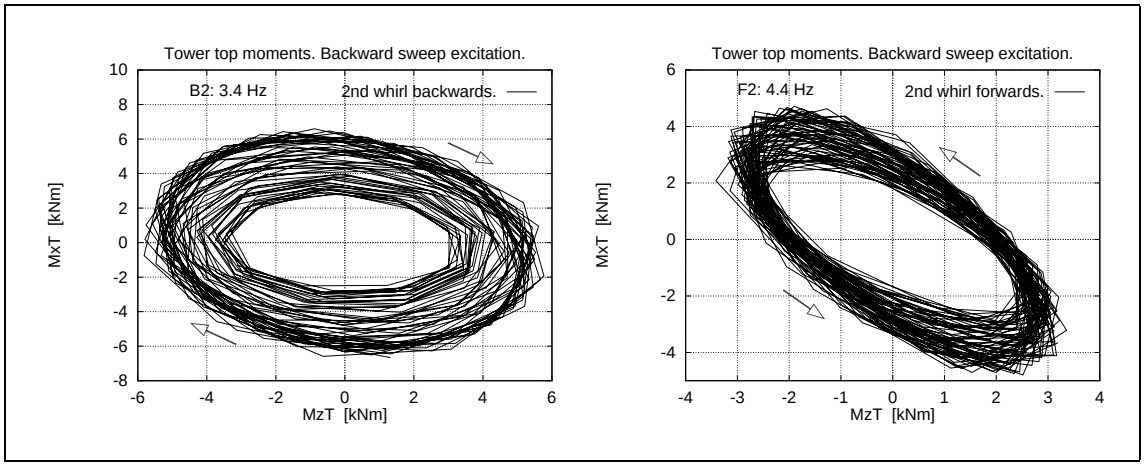

Figure 7.6. Tower top moments during excitation with harmonic moment with linearly varying frequency at the tower top. Tilt moment, M_x^T, and yaw moment, M_z^T. Left: *2^{nd} whirl mode, whirling backwards, 3.4 Hz.* Right: *2^{nd} whirl mode, whirling forwards, 4.4 Hz.*

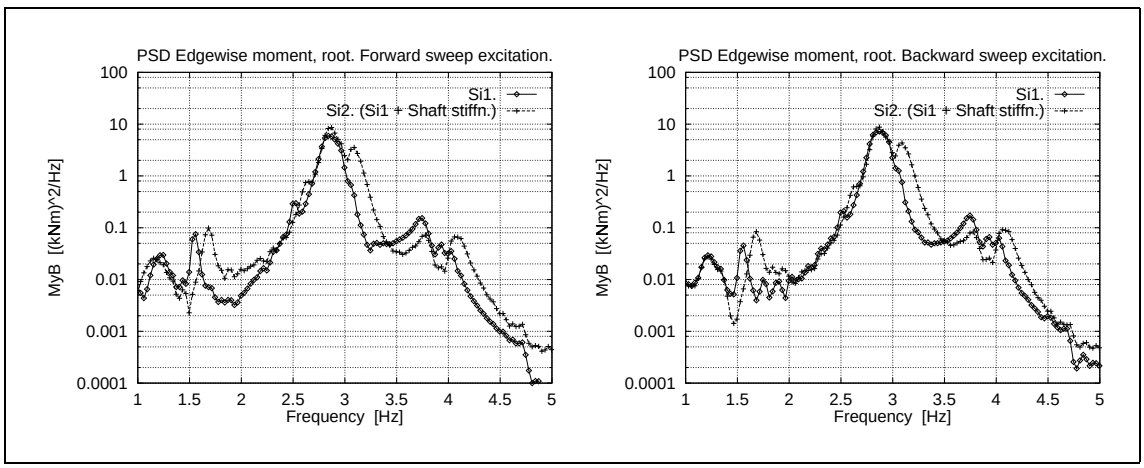

Figure 7.7. Power spectral density of edgewise blade root moment, M_y^B, for whole 10 minutes sweep period. Left: *Forward excitation.* Right: *Backward excitation.*

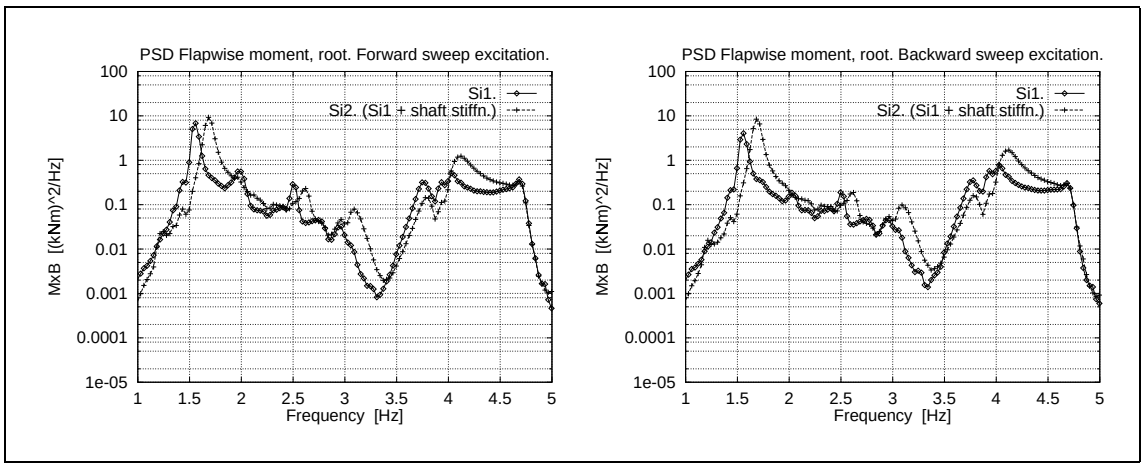

Figure 7.8. Power spectral density of flapwise blade root moment, M_x^B, for whole 10 minutes sweep period. Left: *Forward excitation.* Right: *Backward excitation.*

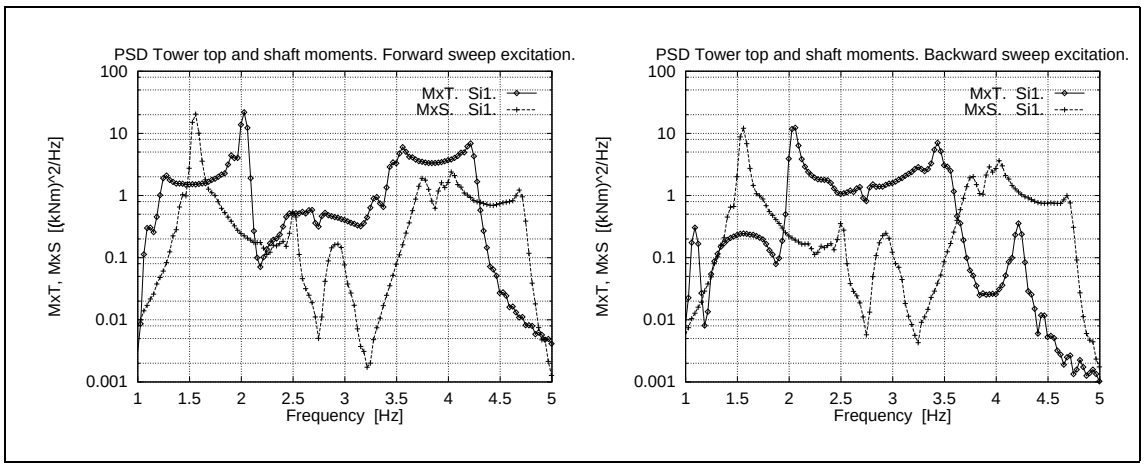

Figure 7.9. Power spectral density of tower top tilt moment, M_x^T, and shaft bending moment, M_x^S, for the whole 10 minutes sweep period. Original shaft stiffness. Left: *Forward excitation.* Right: *Backward excitation.*

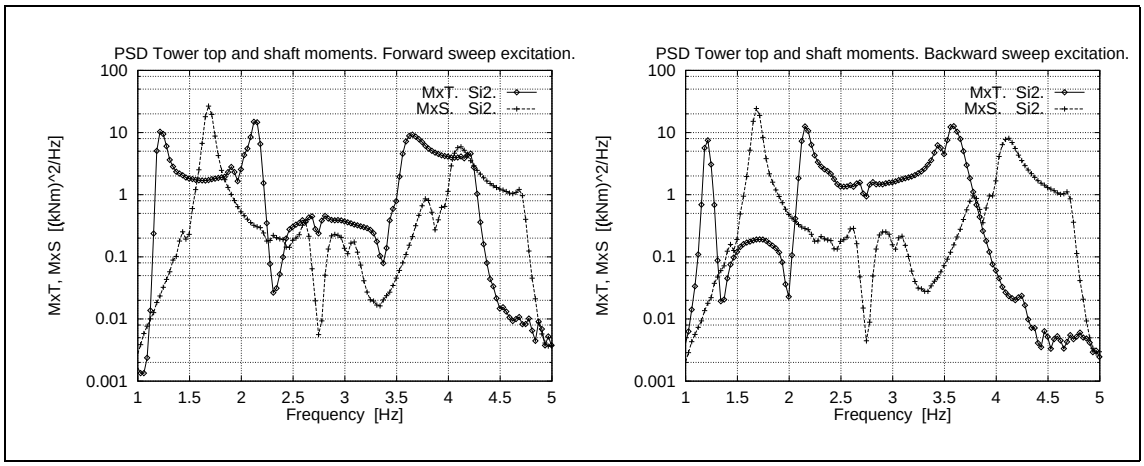

Figure 7.10. Power spectral density of tower top tilt moment, M_x^T, and shaft bending moment, M_x^S, for the whole 10 minutes sweep period. Stiffened shaft. Left: *Forward excitation.* Right: *Backward excitation.*

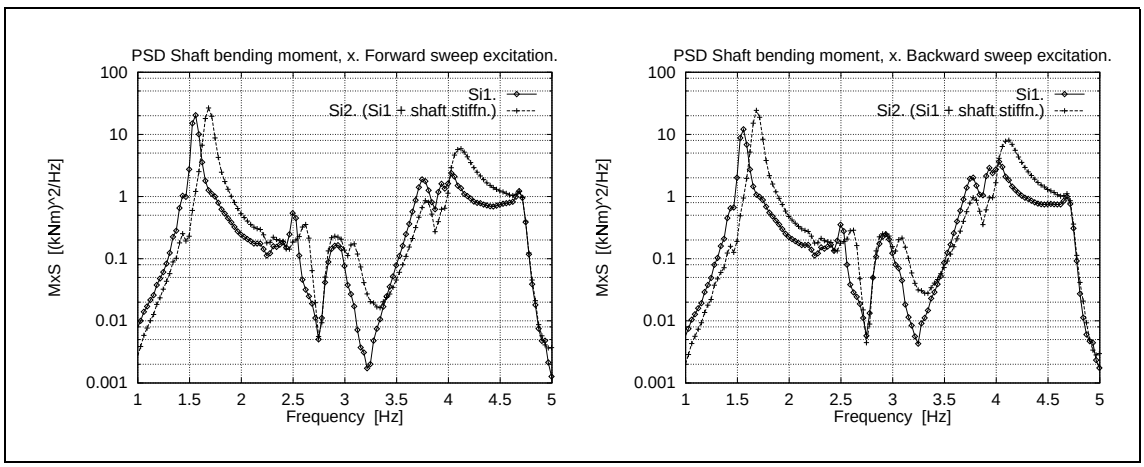

Figure 7.11. Power spectral density of shaft moment, M_x^S, for the whole 10 minutes sweep period. Left: *Forward excitation.* Right: *Backward excitation.*

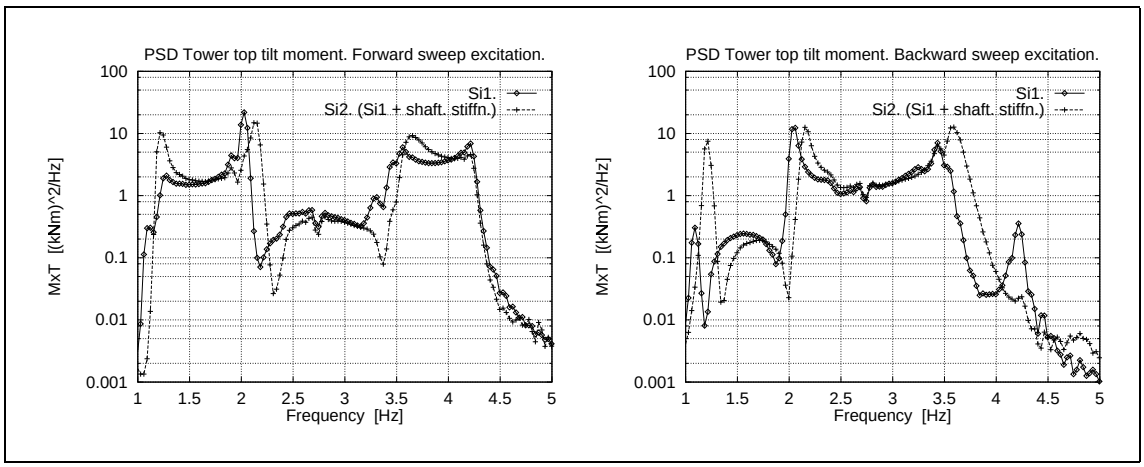

Figure 7.12. Power spectral density of tower top tilt moments, M_x^T, for the whole 10 minutes sweep period. Left: *Forward excitation.* Right: *Backward excitation.*

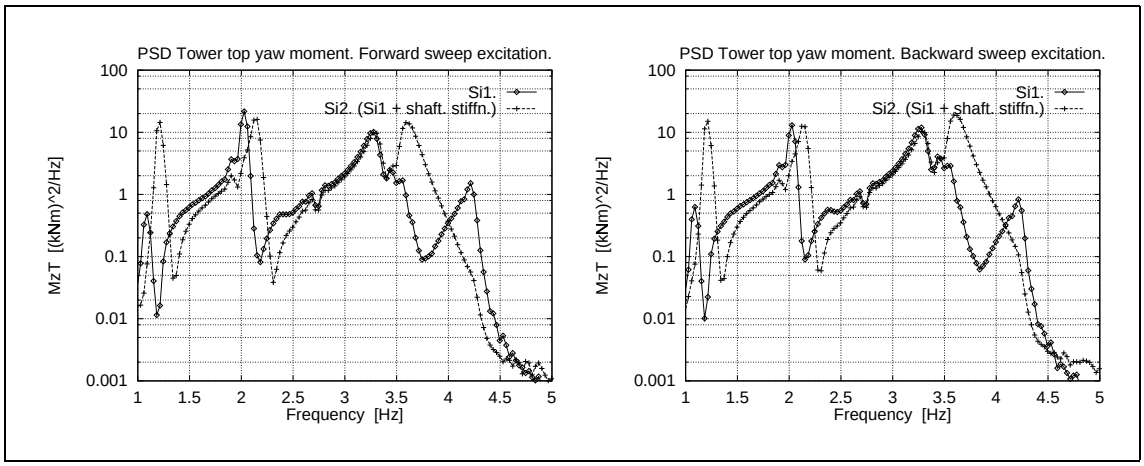

Figure 7.13. Power spectral density of tower top yaw moments, M_z^T, for the whole 10 minutes sweep period. Left: *Forward excitation.* Right: *Backward excitation.*

8 Conclusion

The interaction between edgewise blade vibrations, *local blade whirl*, and the deformation in the rotor tilt-yaw modes during operation, *global rotor whirl*, has been investigated for a 3-bladed wind turbine. The objective is to improve the physical understanding of the interaction by identification of the most important elements of the vibration phenomenon. The problem is simplified by assuming that the dominating inertia force on the blades originates from the edgewise vibration, and that this inertia force can be viewed as an excitation on the yaw and tilt modes.

By applying simple models for the resulting inertia force in the rotor plane and for the movement of the rotor in the tilt-yaw modes, and by additional full aeroelastic calculations without simplifications, it has been illustrated, how a coupling between the local edgewise blade deformations and the global deformations exists. In the presented examples, based on a typical 3-bladed stall regulated wind turbine, the actual value of the frequency of the 2^{nd} backward rotor whirl mode relative to the edgewise blade frequency referred to stationary coordinates has proven to be important for the level of the resulting edgewise blade vibrations. The closer the blade frequency is to the rotor whirl frequency, the easier the vibrations develop. A change of the rotor whirl frequency of approximately 0.2 Hz changes the blade vibration significantly.

However, analysis based on expressions for work shows that the interaction is not a simple resonance phenomenon, as it might seem at first. In the presented examples the energy from an initiated forward local blade whirl vibration can be transferred to the backward blade whirl mode via the 2^{nd} backward rotor whirl mode, when the rotor whirl frequency lies between the forward and the backward blade whirl frequencies. With the rotor whirl frequency outside this range the energy can no longer be exchanged between the two blade whirl modes, and this seems to be important for the development of the vibrations.

This observation suggests that it should be recommended in a design situation to separate the blade whirl frequencies and the rotor whirl frequencies as much as possible, but at the same time the rotor whirl frequency should be kept outside the range limited by the backward and the forward blade whirl frequencies referred to stationary coordinates.

A method based on external excitation and full aeroelastic calculations is presented and proposed as a design tool, which can be used for identification of the rotor whirl frequencies.

It should be stressed that the simplified models for whirl interaction are rather arbitrarily chosen, and the presented description is by no way complete, as the real coupled modes are rather complex due to flexibilities neglected in the simple models, for instance the flapwise blade flexibility. Obviously, we might just as well have looked at the problem the other way around, by showing how an assumed deformation in the tilt-yaw modes would result in an inertia force on the blades in the rotor plane due to the accelerations at the hub. However, the same conclusions would have been obtained. The application of full aeroelastic calculations to support the conclusions is important both in the present work and in a design situation.

Although the presented work is inspired by research on stall regulated wind turbines, and the examples are based on this turbine type, it should be emphasized that the dynamic principles are equally valid for turbines with any type of regulation.

9 References

[1] Petersen, J.T et al. *Prediction of Dynamic Loads and Induced Vibrations in Stall.* Risø report. Risø-R-1045(EN). Risø National Laboratory, Roskilde, Denmark. May 1998.

[2] Madsen, H.Aa. *Forskning i aeroelasticitet. EFP-97 Slutrapport.* Risø rapport. Risø-R-1066(DA). Forskningscenter Risø, August 1998.

[3] Petersen, J.T. *Kinematically Nonlinear Finite Element Model of a Horizontal Axis Wind Turbine.* Ph.D. thesis. Part 1 and 2. Risø National Laboratory. Roskilde, Denmark, July 1990.

[4] Petersen, J.T. *The Aeroelastic Code HawC – Model and Comparisons.* In proceedings of *State of the Art of Aeroelastic Codes for Wind Turbine Calculations.* 28^{th} Meeting of Experts, International Energy Agency, Annex XI. Editor B. Maribo Pedersen, Technical University of Denmark. Lyngby, April 11-12 1996, pp. 129-135.

[5] Petersen, J.T., Rasmussen, F. and Thomsen K. *Kantsvingninger og rotordynamik.* Risø rapport. Risø-I-791(DA). Forskningscenter Risø, Maj 1994.

Bibliographic Data Sheet **Risø-R-1067(EN)**

Title and author(s)

Local Blade Whirl and Global Rotor Whirl Interaction.

Jørgen Thirstrup Petersen, Kenneth Thomsen, Helge Aagaard Madsen

ISBN	ISSN
87–550–2418–1; 87–550–2420–3 (Internet)	0106–2840

Dept. or group	Date
Wind Energy and Atmospheric Physics	August 1998

Groups own reg. number(s)	Project/contract No.
AED 1110013-00	ENS-1363/97-0002

Pages	Tables	Illustrations	References
60	5	45	5

Abstract (Max. 2000 char.)

Investigation of stall induced vibrations has shown that the actual value of the edgewise blade frequency relative to the coupled, global rotor tilt-yaw frequencies is important for development of the vibrations. They develop more easily if the blade frequency is close to one of the rotor tilt-yaw frequencies referred to common coordinates. This observation indicates that an important coupling exists between the blade edgewise modes and the global rotor modes. The presented work aims at providing insight into the physics of this coupling by use of simple models, which take into account the effects believed to be most important in the considered state of operation. We assume that the dominating inertia force on the blades originates from the edgewise vibration. The resulting inertia force at the hub, which turns out to be a force rotating in the rotor plane with the edgewise frequency, is then considered as the forcing on the supporting structure, i.e. the main shaft, the nacelle frame and the tower. A four degrees of freedom model of the rotor and the supporting structure is used to illustrate the global rotor tilt-yaw mode shapes during operation. A mathematical model for the work performed by the inertia force from the blade vibration on the hub movement shows, how energy might be exchanged between the structural elements. In addition, full aeroelastic calculations are used to support and extend the conclusions from the simple models, when the complex, real wind turbine structure is considered. The in-plane inertia force describes an elliptical path in the rotor plane, and we denote the corresponding blade deformation *local blade whirl*. Likewise, the hub moves along an elliptical orbit, when the rotor tilt-yaw modes are excited, and we denote this movement *global rotor whirl*. Using these terms our concern is the interaction between *local blade whirl* and *global rotor whirl*. The models are used to illustrate the findings through examples. It is concluded that not only should the local blade whirl frequencies and the global rotor whirl frequencies be separated as much as possible, but certain frequency intervals should be avoided as well. Although the work is inspired by analysis on stall regulated wind turbines, the dynamic principles are equally valid for turbines with any type of regulation.

Descriptors INIS/EDB

DYNAMIC LOADS; HORIZONTAL AXIS TURBINES; MATHEMATICAL MODELS; MECHANICAL VIBRATIONS; ROTORS; STALL

Available on request from:
Information Service Department, Risø National Laboratory
(Afdelingen for Informationsservice, Forskningscenter Risø)
P.O. Box 49, DK–4000 Roskilde, Denmark
Phone (+45) 46 77 46 77, ext. 4004/4005 · Fax (+45) 46 77 40 13 · Telex 43 116